Journal of the Mechanics and Physics of Solids 57 (2009) 1139–1164

Contents lists available at ScienceDirect

Journal of the Mechanics and Physics of Solids

journal homepage: www.elsevier.com/locate/jmps

Constitutive model for predicting dynamic interactions between soil ejecta and structural panels

V.S. Deshpande [a,*], R.M. McMeeking [a,b], H.N.G. Wadley [c], A.G. Evans [a,b]

[a] Department of Mechanical Engineering, University of California, Santa Barbara, CA 93106, USA
[b] Materials Department, University of California, Santa Barbara, CA 93106, USA
[c] Department of Materials Science and Engineering, University of Virginia, Charlottesville, VA 22904, USA

ARTICLE INFO

Article history:
Received 1 December 2008
Received in revised form
24 April 2009
Accepted 2 May 2009

Keywords:
Granular material
Shock waves
Constitutive
Behaviour
Blast loading

ABSTRACT

A constitutive model is developed for the high-rate deformation of an aggregate comprising of mono-sized spherical particles with a view to developing an understanding of dynamic soil–structure interactions in landmine explosions. The constitutive model accounts for two regimes of behaviour. When the particle assembly is widely dispersed (*regime I*), the contacts between particles are treated as collisions, analogous to those between molecules in a gas or liquid. At high packing densities (*regime II*) the contacts are semi-permanent and consolidation is dominated by particle deformation and inter-particle friction. Regime I is modelled by extending an approach proposed by Bagnold (1954. Experiments on a gravity-free dispersion of large solid particles in a Newtonian fluid under shear. Proceedings of the Royal Society of London A 225, 49–63) to a general strain history comprising volumetric and deviatoric deformation. For regime II, classical soil mechanics models (such as Drucker–Prager) are employed. The overall model is employed to investigate the one-dimensional impact of sand against a rigid stationary target. The calculations illustrate that, unlike single-particle impact, the momentum transmitted to a rigid target is *insensitive to the particle co-efficient of restitution*, but strongly dependent on initial density. The constitutive model is also used to examine the spherical expansion of a shell of sand (both dry and water saturated). In line with initial experimental observations, the wet sand is predicted to form clumps while the dry sand fully disperses. The model shows that this clumping of explosively loaded wet sand exerts higher pressures on nearby targets compared to equivalent dry sand explosions.

1. Introduction

The response of structures to nearby explosions is sensitive to a variety of factors. Among the most important are the intervening medium (air, water, soil) and whether the structure is a solid plate or a sandwich (with two faces separated by a lattice core). Much attention has been devoted to the dynamic response of structures when water and air reside between the panel and the explosion. These assessments have demonstrated the circumstances wherein metallic sandwich designs can outperform solid plates (having the same mass/area) in the sense that the deflections and reaction forces induced by the blast are smaller and the incidence of tearing is diminished (see for example Fleck and Deshpande, 2004; Liang et al.,

* Corresponding author. Current address: Department of Engineering, University of Cambridge, Trumpington Street, Cambridge CB2 1PZ, UK.
E-mail address: vsd@eng.cam.ac.uk (V.S. Deshpande).

0022-5096/$ - see front matter © 2009 Elsevier Ltd. All rights reserved.
doi:10.1016/j.jmps.2009.05.001

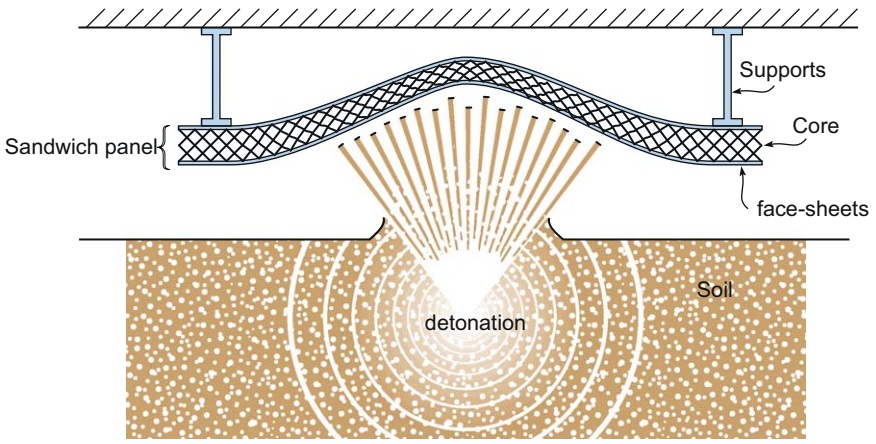

Fig. 1. Sketch of a prototypical problem of a clamped sandwich structure loaded by a shallow mine explosion.

2007; Wei et al., 2008). The benefits arise from two sources. (i) The thinness of the outer face of a sandwich reduces the momentum transmitted to the structure (relative to a thicker solid plate) through a fluid/structure interaction (FSI) effect (Deshpande et al., 2006; Wei et al., 2007; Wadley et al., 2008). This effect is substantial in the case of water blast, but relatively unimportant for air blasts (Noels et al., 2009). (ii) The core can be designed to collapse with a dynamic strength that limits the stress transmitted to the back face, as well as the supports, thereby diminishing the deflections and the reaction forces (Dharmasena et al., 2009a). The corresponding situation for structures subjected to blast from buried landmines is yet to be explored. This objective remains unfulfilled because the available constitutive laws for soil expanding out from a buried explosion do not contain sufficient physics. The intent of the present article is to address this deficiency by developing a basic understanding of the dynamic interaction of soils with structures (Fig. 1).

Detonation of an explosive buried in soil can be divided into the following three temporal phases:

phase I: the detonation of the explosive and the ensuing soil interaction;
phase II: expansion of the gaseous detonation products;
phase III: the development of soil ejecta.

In the first phase, the detonation produces a shock wave in the surrounding soil (Tremblay et al., 1998; Bergeron et al., 1998). When this shock (travelling through the soil) reaches the soil/air interface, it largely reflects as an expansion wave. Only a small fraction of the incident shock is transmitted into air. Namely, the large difference in the acoustic impedance between soil and air causes the resultant air shock to have minimal influence on the target structure (Bergeron and Tremblay, 2000). Consequently, in landmine explosions, the primary loading of the structure is caused by impact of soil, associated with phases II and III.

Experimental characterizations of landmine-blast events have not only established key phenomena occurring within the relevant phases (Bergeron et al., 1998; Braid, 2001; Weckert and Andersen, 2006; Neuberger et al., 2007) but also led to empirical models for quantifying the impulsive loads generated by landmines (Westine et al., 1985), as well as the construction of design-for-survivability codes (Morris, 1993). These models continue to be of great value. However, they are restricted to situations close to those used for calibrations and cannot be extrapolated to either different soil types or, more importantly, to sandwich designs (Fig. 1). A physics-based model for soil is needed to progress toward the desired objective.

Recent advances in numerical analysis capabilities, particularly the coupling of Eulerian and Lagrangian solvers, have created the possibility of conducting simulations of complex loadings created by blasts. Success is dependent on the availability of constitutive models for dispersing and compacting soils under extreme dynamic loadings (see Johnson (1971) for a review of explosive excavation and Grujicic et al. (2008) for a detailed analysis of soil models used to simulate landmine explosions). The existing approaches are based on one of two representations: (a) the so-called three-phase model (Wang and Lu, 2003; Wang et al., 2004), which is a modification of Drucker and Prager (1952) or (b) the *porous-material/compaction* model (Laine and Sandvik, 2001), which is widely used in design codes. Recent updates by Grujicic et al. (2006) that include the effect of moisture have illustrated its applicability (Grujicic et al., 2008) by comparing predictions of blast impulse with data from Bergeron and Tremblay (2000) and Foedinger (2005). Still, discrepancies between measurements and predictions persist. Moreover, some of the basic physics is lacking, because these models are restricted to a soil packing density sufficiently high that particle–particle contacts are semi-permanent. Thus, while these models are appropriate in the initial stages of a landmine explosion, their applicability when loose ejecta are formed is questionable.

The aim of this paper is to develop an alternative approach that captures the dynamic response of soils over their entire range of states, ranging from dense-packed to low-density sprays or ejecta. The outline is as follows. First we summarize the physics of a landmine explosion. Second, a three-dimensional (3D) constitutive model for the dynamic response of mono-disperse spheres is developed, based on the classical analysis of Bagnold (1954). Finally, the constitutive model is employed in two example one-dimensional (1D) problems that illuminate the key phenomena governing landmine explosions and the interaction of soil ejecta with structures: (a) the response of sand impacting a rigid wall and (b) the explosive expansion of a spherical shell of sand. For a preliminary validation of the model, 3D coupled Eulerian/Lagrangian predictions of the deflections of plates impacted by a spherically expanding sand shell are compared with experimental measurements presented in a companion paper (Dharmasena et al., 2009b).

2. Synopsis of the physics of a mine explosion

The energy released by explosions takes many forms: heat, kinetic energy of air and soil, soil deformation and work done by the expanding gaseous products. The limiting cases are as follows. (i) At one extreme, if an explosion occurs deep underground, the energy is totally absorbed by soil compression and deformation. The detonation products are contained and no air shock is generated. This is called *camouflet*. (ii) At the other, surface detonation of a mine on, say, frozen soil transmits very little energy to the ground and the deformation induced in nearby structures is caused by the expanding detonation products and air shock. Between these limiting cases, a broad range of conditions exist wherein a substantial portion of the available energy is transmitted as soil kinetic energy, thereby generating "ejecta". The ejecta may carry considerable momentum capable of severely damaging a nearby structure. Developing an understanding of the response of the soil in this intermediate situation is the primary focus of this article.

Flash X-ray images of a (100 g C4) mine buried 8 cm under dry sand illustrate that, initially, the soil expands as a hemisphere (Fig. 2a), followed by an inverted cone of ejecta (Fig. 2b; Bergeron et al., 1998). In the time domain, the complete event may be divided into three distinct phases. *Phase I—Early interaction with the soil.* When the explosion is

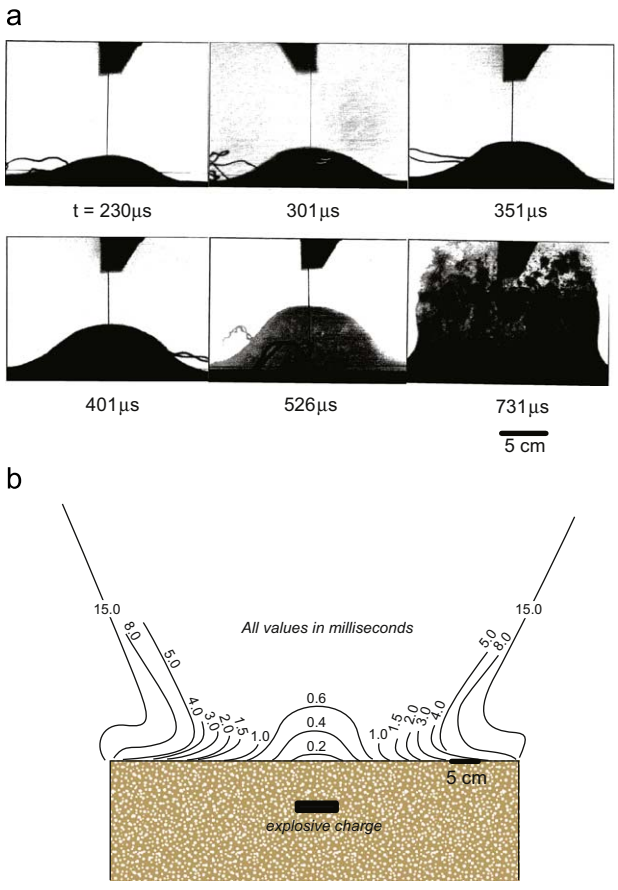

Fig. 2. (a) Flash X-ray images of phase II and (b) sequential traces of the ejecta of the explosion of a 100 g C4 mine buried 8 cm under type A dry sand. Time $t = 0$ corresponds to the detonation of the explosive. Adapted from Bergeron et al. (1998).

initiated, a detonation wave transforms the (usually) solid explosive into gaseous detonation products. Three zones of deformation emanate from the centre. (i) A zone of crushing near the centre, where pressure and temperature are so high that shock transmission is independent of the physical structure of the soil. This zone extends from $2R_e$ to $3R_e$ (where R_e is the charge radius) (Bangash, 1993). (ii) Further away, from $3R_e$ to $6R_e$, the soil deforms plastically by irreversible crushing and collapse (Drake and Little, 1983). (iii) Beyond $6R_e$, the response is elastic with shock transmission resulting in reversible deformation of the soil. Three types of stress wave are induced: compression (p), shear (s), and Rayleigh (R). The p and s waves expand in a spherical manner with amplitude that decreases as r^{-2} (where r is the distance from the source). The Rayleigh waves expand on a cylindrical front and decay as $r^{-1/2}$. Their rate of decay is a strong function of the physical properties of the soil. For example, the ground shock intensity can vary by up to two orders of magnitude between dry soil and saturated clay. This early phase determines the amount of energy available to convert to kinetic energy of the soil. It is affected by the depth of burial, soil properties, and soil moisture content. *Phase II—Gas expansion*. When the compressive wave reaches the soil–air interface, it is partly transmitted to air as a shock, but mostly reflected back toward the centre as a tensile wave. The latter combines with the push by the high-pressure detonation products to hemispherically expand the soil into the surrounding air (Fig. 2a), which eventually results in ejection of a soil cap. This process occurs within a few milliseconds. *Phase III—Soil ejecta*. The high-pressure gas in the soil continues to do work on the walls of the cavity created by the explosion. Soil continues to be eroded and ejected at high speed for tens (sometimes hundreds) of milliseconds. The trajectory of the associated ejecta is generally in the upward direction, within an inverse cone having included angle (between 60° and 90°; Fig. 2b) that increases with either decreasing depth of burial or looser soil.

The processes described above suggest that two distinct types of soil behaviour need to be understood: (i) compaction during the early stages of the event and (ii) expansion of the loose soil within a hemispherical cap, which later erodes from the walls of the cavity. The first can be addressed using the large body of work on the dynamics of dense soils [the well-established Drucker and Prager (1952), Mohr–Coulomb (Muir Wood, 1990), and Cam–Clay (Roscoe et al., 1958) models]. The focus of this study is on the second process, involving the response of a loose aggregate, particularly relevant to ejecta from shallow-buried explosives and the loading of structures by high-velocity sprays of low-density soil.

3. Constitutive model development

The mechanical response of a flowing granular material is governed by forces exerted at the many points of contact between particles. When the assembly is widely spaced and in vigorous motion, individual contacts are of short duration and may be treated as ''collisions'', analogous to encounters between molecules in a liquid or gas. This response was first analysed by Bagnold (1954), and referred to as *regime I*. As the packing density of the assembly increases, the contacts become semi-permanent. This is the response analysed by most consolidation-type soil mechanics models, and referred to as *regime II*. Everything between these extremes is possible and of interest. The present objective is to develop a straightforward constitutive model that spans both regimes. We begin by addressing regime I and then propose a model that spans both.

3.1. A model characterizing regime I

The model has been developed using a step-wise approach in accordance with the following sequence (Fig. 3). In the first step, the fundamentals of particle contacts are examined with the objective of relating the collision time between particles, t_c, and co-efficient of restitution e to the particle mass, m_p, and the properties of the contact (viz. the damping constant C and spring constant K_n). In a second step, dimensional analysis is used to identify two limiting responses: (i) inertia dominated and (ii) domination by the interaction of particles. Next, insights from this dimensional analysis are used to extend the Bagnold (1954) model to account for volumetric straining of the granular assembly and for small values of the co-efficient of restitution e. In the fourth step, the two-dimensional (2D) analysis is used to propose a phenomenological 3D representation, which becomes the basis for the ensuing computations.

Particle interactions. The rheology of granular flows is strongly influenced by the dynamics of particle–particle interactions. Early work invoked a *hard particle model* comprising instantaneous, binary collisions between particles (for example, Campbell and Brennen, 1985). However, the high shear rates required to achieve such flow conditions are unusual (Campbell, 2002) and most practical granular flows involve complex particle–particle interactions. To illustrate, we examine the interactions most often used in computer simulations, referred to as the *soft particle model* (Fig. 3a). First utilized by Cundall and Strack (1979), this (admittedly simplistic) model consists of a linear spring K_n, and dashpot C, governing the normal motion with another linear spring K_s, and a Coulomb friction co-efficient μ, governing the tangential motion. The normal and tangential contact forces are

$$F_n = K_n\delta_n + C\dot{\delta}_n \tag{3.1}$$

and

$$F_s = \begin{cases} -K_s\delta_s & \text{if } |F_s| < |\mu F_n| \\ -\mu|F_n|sign(\delta_s) & \text{otherwise} \end{cases}, \tag{3.2}$$

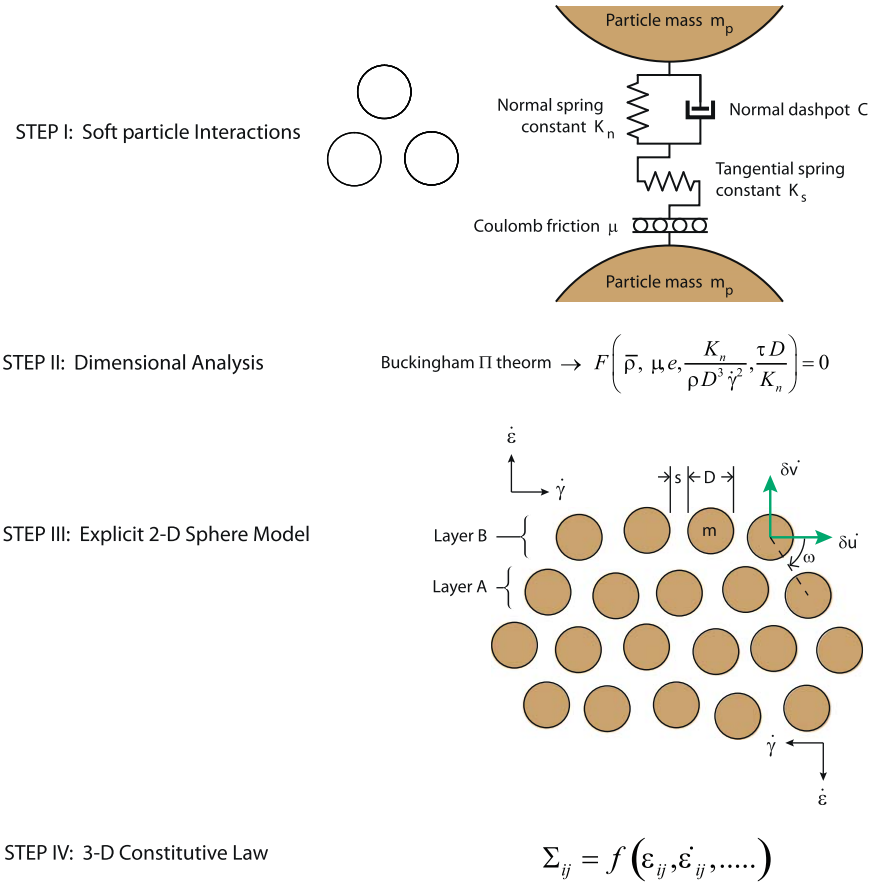

Fig. 3. The four steps used in the development of the constitutive law. (a) Step I: schematic of the soft particle model of particle interactions. (b) Step II: the non-dimensional analysis. (c) Step III: the assemblage of mono-sized spheres used in the two-dimensional generalisation of the Bagnold (1954) analysis. (d) Step IV: the 3D generalization of the model.

respectively, where δ_n and δ_s are the relative normal and tangential displacements of the contacting particles. The Poisson's ratio of the solid is related to the ratio K_s/K_n (Bathurst and Rothenburg, 1988), while K_n is a function of the Young's modulus. Furthermore, the dashpot constant C determines the loss of energy during normal collisions and is directly related to the co-efficient of restitution e for normal collisions. Consequently, appropriate values of C can be determined from the known or measured co-efficients of restitution by means of the relation

$$e = \exp\left[-\frac{\pi C}{(2m_p K_n - C^2)^{1/2}}\right], \tag{3.3}$$

where m_p is the particle mass. This model leads to a collision time for individual binary collisions:

$$t_c = \frac{\pi m_p}{[2m_p K_n - C^2]^{1/2}} = -m_p \frac{\ln(e)}{C}. \tag{3.4}$$

In the limit of plastic collisions (with $e \to 0$), $t_c \to \infty$. Thus, the simple model has the attractive feature that the contact properties can be readily related to the co-efficient of restitution e. *This is the result carried forward into the ensuing constitutive formulation.*

Dimensional analysis. Given the foregoing particle interaction model, characterized by a set of parameters (K_n, e, μ), the stress τ in a typical shearing flow, with a shear strain rate $\dot{\gamma}$, can be related to these parameters, plus $(D, \rho, \bar{\rho})$ [where ρ and D are the solid particle density and particle diameter, respectively, with $\bar{\rho}$ the solid volume fraction]. Through dimensional analysis (Campbell, 2002)

$$\frac{\tau D}{K_n} = f\left(\bar{\rho}, \mu, e, \frac{K_n}{\rho D^3 \dot{\gamma}^2}\right). \tag{3.5}$$

Such a construct demonstrates the importance of the parameter $K_n/\rho D^3 \dot{\gamma}^2$, which may be interpreted as (the square of) the ratio of the time between collisions $t_{shear} = 1/\dot{\gamma}$, to the collision time, t_c, which scales as $(m_p/K_n)^{1/2}$. These considerations

suggest two asymptotic flow states. The first is identified by instantaneous (necessarily binary) collisions in which $t_c \ll t_{shear}$. We refer to this as the *inertial domain*. Its rheology is independent of the stiffness K_n and thus $K_n/\rho D^3\dot{\gamma}^2$ must disappear as a parameter, leaving

$$\frac{\tau}{\rho D^2\dot{\gamma}^2} = f_1(\bar{\rho}, \mu, e). \tag{3.6}$$

This is the form that Bagnold (1954) surmised in his classic and much quoted paper on granular shear flows. The second asymptotic domain is characterized by long contact times, $t_c \gg t_{shear}$, wherein the particles are forced to interact with a frequency comparable to the binary collision time. Consequently multiple particle interactions occur, causing force chains to form. This rheology is independent of the shear rate $\dot{\gamma}$ so that the stress is again independent of $K_n/\rho D^3\dot{\gamma}^2$ and dimensional analysis suggests

$$\frac{\tau D}{K_n} = f_2(\bar{\rho}, \mu, e). \tag{3.7}$$

Note that $\tau D/K_n$ is the deformation induced in the particles by the stress τ, whereupon this is referred to an *elastic quasi-static domain*. Somewhere between these limits lies the *elastic–inertial domain*, wherein $K_n/\rho D^3\dot{\gamma}^2$ remains as a parameter. Computer simulations would be needed to map out these domains (Campbell, 2002, 2003). Such simulations are not required for present purposes, since *the only aspect of the foregoing results needed in the ensuing analysis is that, in the limit of plastic collisions ($t_c \gg t_{shear}$), the response is independent of strain rate*.

Explicit 2D Model for mono-sized spheres. En-route to deriving a constitutive law, we pursue an explicit 2D analysis of an aggregate of mono-sized spheres (Fig. 3c). For this purpose we modify the Bagnold analysis (neglecting the effects of temperature changes, see Appendix A1), to approximately account for: (i) volumetric straining of the granular assembly and (ii) small values of the co-efficient of restitution e (when $t_c \gg t_{shear}$). The particle assemblage is subjected to shear and normal strain rates $\dot{\gamma}$ and $\dot{\varepsilon}$, respectively. The particles, diameter D, are spaced d apart. Their linear concentration, $\lambda \equiv D/d$, is related to the volume fraction $\bar{\rho}$ of the particles by

$$\lambda \equiv \frac{D}{d} = \frac{1}{(\bar{\rho}_{max}/\bar{\rho})^{1/3} - 1}, \tag{3.8}$$

where $\bar{\rho}_{max} = 0.74$ is the maximum packing density of mono-sized spheres. The horizontal and vertical velocities of particles in layer A relative to the adjacent layer B (Fig. 3c) are

$$\delta\dot{u} = (d + D)\dot{\gamma} \tag{3.9}$$

and

$$\delta\dot{v} = (d + D)\dot{\varepsilon}, \tag{3.10}$$

respectively. The average number of collisions per unit time is $f(e, \lambda)\delta\dot{u}/d$, where $f(e, \lambda)$ is a dimensionless constant to be specified subsequently. The rate of collisions is dependent on concentration, with the probability of collisions increasing with increasing λ (Bagnold, 1954). We add a dependence on the co-efficient of restitution e motivated by the foregoing particle interaction result (Eq. (3.4)) as follows. The change in momentum of particles in layer A per collision is $(1 + e)m(\delta\dot{u}\cos\omega - \delta\dot{v}\sin\omega)$, where ω is an angle dependent on the collision conditions. The repulsive pressure between the layers is

$$\begin{aligned} p &= \frac{f(e, \lambda)\delta\dot{u}}{d}\frac{m(1 + e)}{(d + D)^2}(\delta\dot{u}\cos\omega - \delta\dot{v}\sin\omega)\sin\omega \\ &= \zeta f(e, \lambda)\rho D^2\lambda\dot{\gamma}(\dot{\gamma}\cos\omega - \dot{\varepsilon}\sin\omega)\sin\omega \end{aligned} \tag{3.11}$$

where $\zeta = \pi(1+e)/6$. The grains do not collide if $\dot{\gamma}\cos\omega - \dot{\varepsilon}\sin\omega < 0$ and, in these circumstances, the pressure $p = 0$. The shear stress corresponding to this repulsive pressure is

$$\tau = p\cot\omega. \tag{3.12}$$

The basic forms for the stress and strain rate relations expressed in (3.11) and (3.12) are generalized to a 3D setting in the next step.

Phenomenological 3D generalized constitutive law. We use the preceding analysis to motivate a phenomenological 3D constitutive model for an aggregate of mono-sized spheres subjected to a strain rate $\dot{\varepsilon}_{ij}$. In the 3D setting, we identify the foregoing shear $\dot{\gamma}$ and normal $\dot{\varepsilon}$ strain rates with the von-Mises $\dot{\varepsilon}_e$ and volumetric $\dot{\varepsilon}_m$ rates, respectively. The strain rates $\dot{\varepsilon}_e$ and $\dot{\varepsilon}_m$ are defined as

$$\dot{\varepsilon}_e = \left(\frac{2}{3}\dot{\varepsilon}'_{ij}\dot{\varepsilon}'_{ij}\right)^{1/2} \tag{3.13}$$

and

$$\dot{\varepsilon}_m = \dot{\varepsilon}_{kk}, \tag{3.14}$$

where $\dot{\varepsilon}'_{ij} = \dot{\varepsilon}_{ij} - \delta_{ij}\dot{\varepsilon}_m/3$ and δ_{ij} is the Kronecker delta. Based on the 2D analysis we define an effective strain rate

$$\dot{\varepsilon}_f = \alpha\dot{\varepsilon}_e - \beta\dot{\varepsilon}_m, \tag{3.15}$$

where we replace $\cos\omega$ and $\sin\omega$ with the co-efficients α and β, respectively. The expressions equivalent to (3.11) and (3.12) are then given by

$$\sigma_m \equiv \frac{\sigma_{kk}}{3} = \begin{cases} -\beta g\dot{\varepsilon}_e\dot{\varepsilon}_f & \text{if } \dot{\varepsilon}_f > 0 \\ 0 & \text{otherwise} \end{cases}, \tag{3.16}$$

$$\sigma_e \equiv \sqrt{\frac{3}{2}S_{ij}S_{ij}} = -\frac{\alpha}{\beta}\sigma_m, \tag{3.17}$$

where $S_{ij} \equiv \sigma_{ij} - \sigma_m\delta_{ij}$ and the constant g is defined as

$$g \equiv f(e,\lambda)\lambda\zeta\rho D^2. \tag{3.18}$$

The components of the stress tensor consistent with these expressions follow as

$$\sigma^D_{ij} = \begin{cases} \frac{2}{3}\alpha g\dot{\varepsilon}_f\dot{\varepsilon}'_{ij} + \delta_{ij}\sigma_m & \text{if } \dot{\varepsilon}_f > 0 \\ 0 & \text{otherwise} \end{cases}, \tag{3.19}$$

where the superscript "D" signifies dynamic stresses due to grain micro-inertia.

It remains to specify the functional $f(e,\lambda)$. The experiments of Bagnold (1954) implied that the stresses decrease as the square of the separation distance between particles, $f(e,\lambda) \propto \lambda$. Since there are no guidelines for selecting the dependence on e (neither experimental nor computational) *we propose a form that needs to be validated*. The foregoing dimensional analysis suggests that, in the limit of plastic collisions ($t_c \gg t_{shear}$), the response should be independent of strain rate. Consistent with these arguments we postulate a form

$$f(e,\lambda) = e\lambda. \tag{3.20}$$

Substituting Eq. (3.20) into Eq. (3.19), the dynamic stresses due to grain inertia effects become

$$\sigma^D_{ij} = \begin{cases} e\lambda^2\zeta\rho D^2\dot{\varepsilon}_f\left(\frac{2}{3}\alpha\dot{\varepsilon}'_{ij} - \delta_{ij}\beta\dot{\varepsilon}_e\right) & \text{if } \dot{\varepsilon}_f > 0 \\ 0 & \text{otherwise} \end{cases}. \tag{3.21}$$

The merits of this representation and of the choice of the functional (3.20) are assessed in Section 5, on comparing predicted plate deflections with experimental measurements (Dharmasena et al., 2009b).

3.2. A combined constitutive model

Above a critical relative density $\bar{\rho}_{crit}$, the contacts between the particles become semi-permanent, whereupon the overall stress state has contributions from both consolidation and micro-inertia. We specify that the total stress is the sum of these contributions:

$$\sigma_{ij} = \begin{cases} \sigma^D_{ij} + \sigma^c_{ij} & \text{if } \bar{\rho} \geq \bar{\rho}_{crit} \\ \sigma^D_{ij} & \text{otherwise} \end{cases}, \tag{3.22}$$

where σ^c_{ij} are the stresses associated with consolidation of the aggregate, specified via any standard soil consolidation model, e.g. a visco-plastic, Drucker–Prager-type model as detailed in Appendix B1.

In this study, the focus is on the micro-inertial stresses and so the simplest consolidation model is employed wherein the consolidating aggregate is assumed to undergo isotropic elastic deformations with a bulk modulus κ and zero shear modulus. The consolidation stresses are then given as

$$\sigma^c_{ij} = \begin{cases} \delta_{ij}\kappa\left[\varepsilon_m - \ln\left(\frac{\bar{\rho}_{init}}{\bar{\rho}_{crit}}\right)\right] & \text{if } \varepsilon_m < \ln\left(\frac{\bar{\rho}_{init}}{\bar{\rho}_{crit}}\right) \\ 0 & \text{otherwise} \end{cases}, \tag{3.23}$$

where $\bar{\rho}_{init}$ is the initial volume fraction of the aggregate and ε_m the logarithmic volumetric strain measured with respect to the initial state.

We complete the constitutive description by specifying an evolution relation for $\bar{\rho}$. Recall that, prior to consolidation, the particles do not compress, such that the volumetric compression of the aggregate increases $\bar{\rho}$. Once consolidation commences, the particles compress and $\bar{\rho}$ is expected to remain approximately constant. We thus approximate the $\bar{\rho}$ versus

ε_m relation as

$$\bar{\rho} = \begin{cases} \bar{\rho}_{init} \exp(-\varepsilon_m) & \varepsilon_m > \ln\left(\dfrac{\bar{\rho}_{init}}{\bar{\rho}_{crit}}\right) \\ \bar{\rho}_{crit} & \text{otherwise} \end{cases}. \tag{3.24}$$

In order to implement this model, the following input parameters are needed: particle diameter D, particle density ρ, critical volume fraction $\bar{\rho}_{crit}$, $\bar{\rho}_{max} = 0.74$, the Bagnold parameters (α, β), the bulk modulus of the aggregate κ, the co-efficient of restitution e, and the initial density $\bar{\rho}_{init}$. Their selection is elaborated below.

4. One-dimensional impact against a stationary target

To illustrate some of the important physics embodied in the constitutive law, we analyze the 1D impact of a slug of sand against a stationary target (Fig. 4). The one dimensionality implies that the sand compacts against the target with no lateral

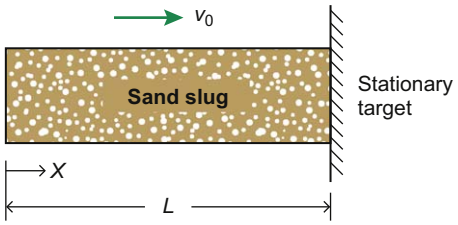

Fig. 4. Sketch of the one-dimensional impact of a sand slug against a rigid stationary target. The co-ordinate X used to define the position of a material point in the un-deformed configuration is indicated.

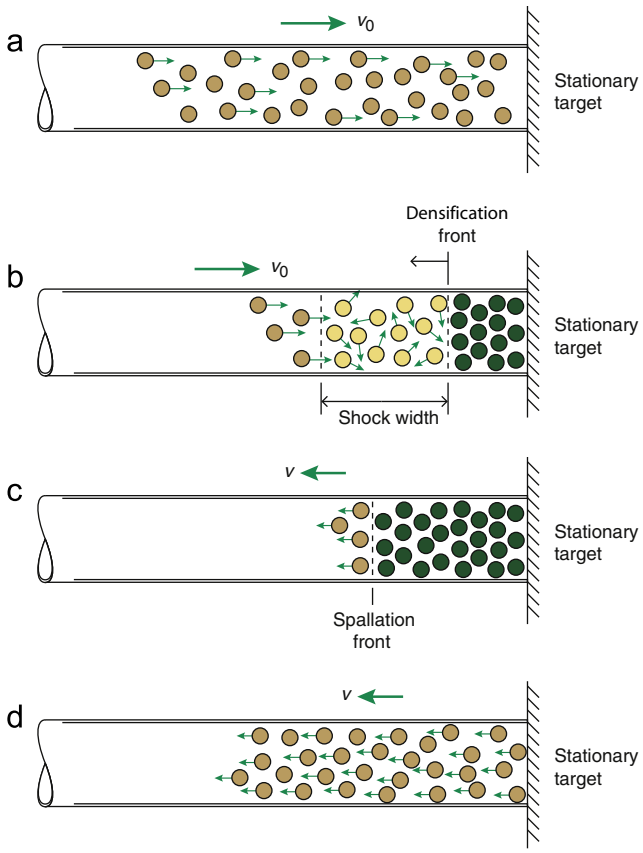

Fig. 5. Sketches of a low relative density assemblage of mono-sized spheres impacting a rigid target. Lateral expansion of the assemblage is prevented by a cylindrical tube. (a) Just prior to impact. (b) The partially densified assemblage with the densification front moving in the opposite direction to the initial particle velocity. (c) The compressive densification front reflects from the free edge of the assemblage as a tensile wave, causing reflection (spallation) of the particles. (d) This tensile front travels through the assemblage and reaches the target. At this point all the particles now have a velocity opposite in direction to their initial velocity. The width of the densification shock front is indicated in (b).

spreading—thought to be representative of the response near the centre of a panel impacted by a spray of sand (Fig. 1). The relevant phenomena are described before proceeding with numerical simulations. When a slug comprising a loose aggregate of particles impacts the target (Fig. 5a), it densifies against the target with a densification front moving in the opposite direction to the slug (Fig. 5b). In the transition zone between the loose to dense regions (Fig. 5b), significant energy is dissipated through repeated collisions of the particles. When the densification front reaches the distal (free) surface, it reflects as a tensile wave, resulting in reflection of the aggregate (Fig. 5c), referred to as spallation. This tensile wave traverses through the slug, causing all of the particles to reflect (Fig. 5d). The associated residual momentum of the particles governs the momentum transmitted to the target.

The calculations conducted for this problem use an explicit finite-deformation finite-element method with no artificial damping. Approximately 120 1D constant strain elements were employed. The initial and boundary conditions were specified as follows. The sand slug was given a spatially uniform initial velocity v_o in the positive x_1-direction with contact between the rigid wall and the sand modelled via a penalty contact method. The 1D elements model uniaxial straining of the sand with the element strain $\varepsilon \equiv \varepsilon_{11}$ and all other strain components set to zero. All calculations are for a slug having mass per unit area $m = 8\,\mathrm{kg\,m^{-2}}$ (slug length $L = m/(\rho\bar{\rho}_{init})$). The following material properties are used: particle diameter $D = 200\,\mu\mathrm{m}$, $\rho = 2700\,\mathrm{kg\,m^{-3}}$ (corresponding to silica), critical volume fraction $\bar{\rho}_{crit} = 0.65$, with parameters $\alpha = 0.1$, $\beta = 0.3$ estimated from the experimental data presented in Bagnold (1954). The bulk modulus of the aggregate was

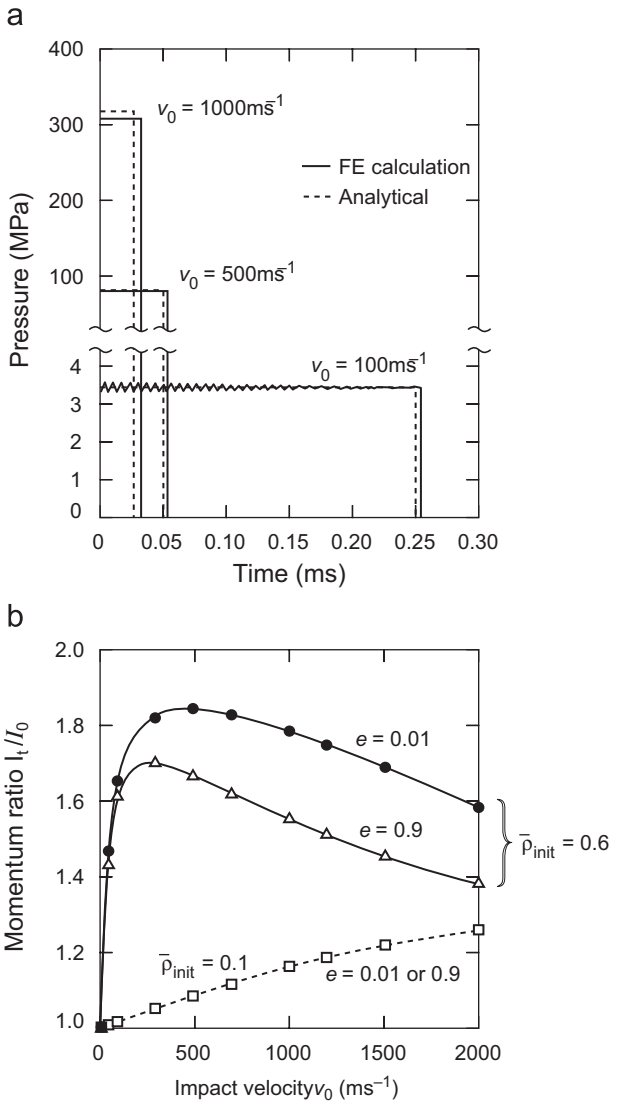

Fig. 6. Finite-element predictions of (a) the pressure $p_t(t)$ exerted by a $\bar{\rho}_{init} = 0.1$ sand slug on a stationary target for selected values of the impact velocity v_o and co-efficient of restitution $e = 0.9$ (results with $e = 0.01$ are indistinguishable). (b) The ratio of the transmitted to initial momentum, I_t/I_0, as a function of impact velocity for sand slugs with $\bar{\rho}_{init} = 0.1$ and 0.65. For comparison purposes we include analytical predictions of the pressure traces (Appendix C) in (a).

estimated as follows. The p-wave wave speed in dry sand is, $c_p \approx 1000\,\mathrm{m\,s^{-1}}$ (Press, 1966). Recall that the bulk modulus is related to this speed by $\kappa = c_p^2 \rho_s$, which implies that $\kappa = 1.7\,\mathrm{GPa}$. Given these parameters, in the ensuing assessment the respective roles of the co-efficient of restitution e and the initial packing density $\bar{\rho}_{init}$ of the sand are examined.

Influence of co-efficient of restitution. Predictions of time variation of the pressure p_t exerted by a sand slug (initial relative density $\bar{\rho}_{init} = 0.1$) on a stationary target are plotted in Fig. 6a for two values of co-efficient of restitution, $e = 0.9$ and 0.01, and three choices of impact velocity v_o (time $t = 0$ is defined as the instant when the slug impacts the target). The impact exerts a rectangular pulse on the target with a pressure that increases with increasing v_o, *but relatively insensitive to e*. The corollary is that the momentum transmitted to the target

$$I_t = \int_0^\infty p_t \, dt \tag{4.1}$$

is also insensitive to e, with $I_t/I_0 \approx 1$, as illustrated in Fig. 6b. This feature implies that all of the kinetic energy of the sand is dissipated by collisions between particles, in stark contrast to that for a single particle impacting a stationary target, wherein the transmitted momentum is $I_t/I_0 = 1+e$.

In order to understand the differences between the two situations we explore the sand impact results in greater detail. The normalised velocity distributions at selected times after impact (at $v_o = 1000\,\mathrm{m\,s^{-1}}$) are shown in Fig. 7 (for $e = 0.9$ and 0.01). The corresponding distributions of the relative density $\bar{\rho}$ are included in Fig. 8. The spatial distributions are plotted in the un-deformed configuration with $x = 0$ corresponding to the impact surface and $x = L$, the distal end. The following sequence of events is apparent, consistent with the sketches in Fig. 5: (i) upon impact, the sand in contact with the target comes to rest and densifies to $\bar{\rho}_{crit}$; (ii) the densification front propagates backward through the sand and reaches the distal end at $t \approx 14\,\mu\mathrm{s}$; (iii) thereafter, this compression front reflects from the free surface as a tensile wave, resulting in spallation

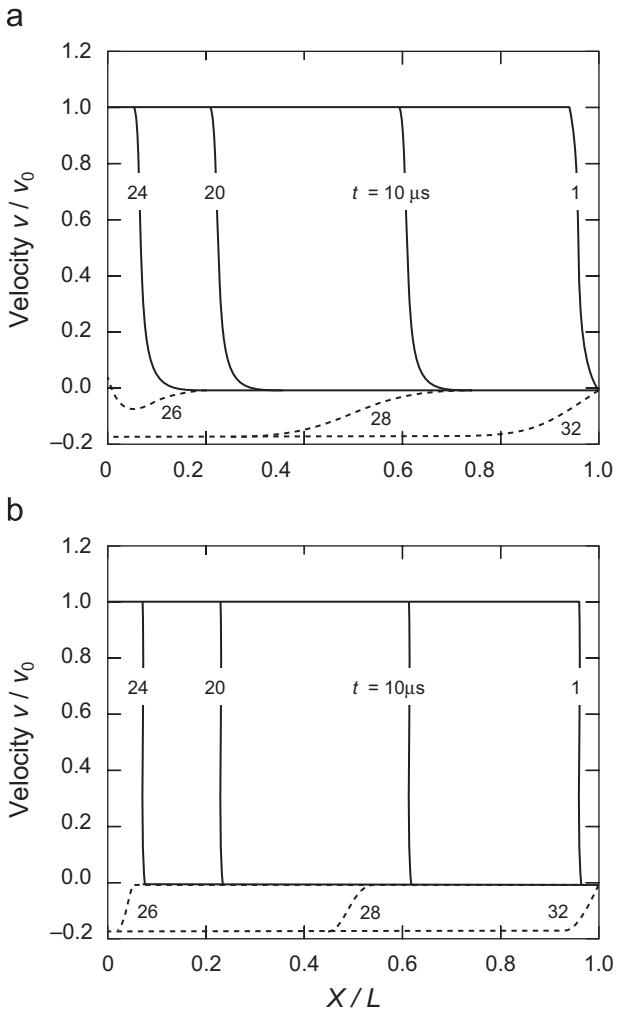

Fig. 7. Normalised particle velocity distributions in the $\bar{\rho}_{init} = 0.1$ sand slug at selected times after impact ($v_o = 1000\,\mathrm{m\,s^{-1}}$) for (a) $e = 0.9$ and (b) $e = 0.01$. The spatial distributions are plotted in the un-deformed configuration with the co-ordinate X defined in Fig. 4.

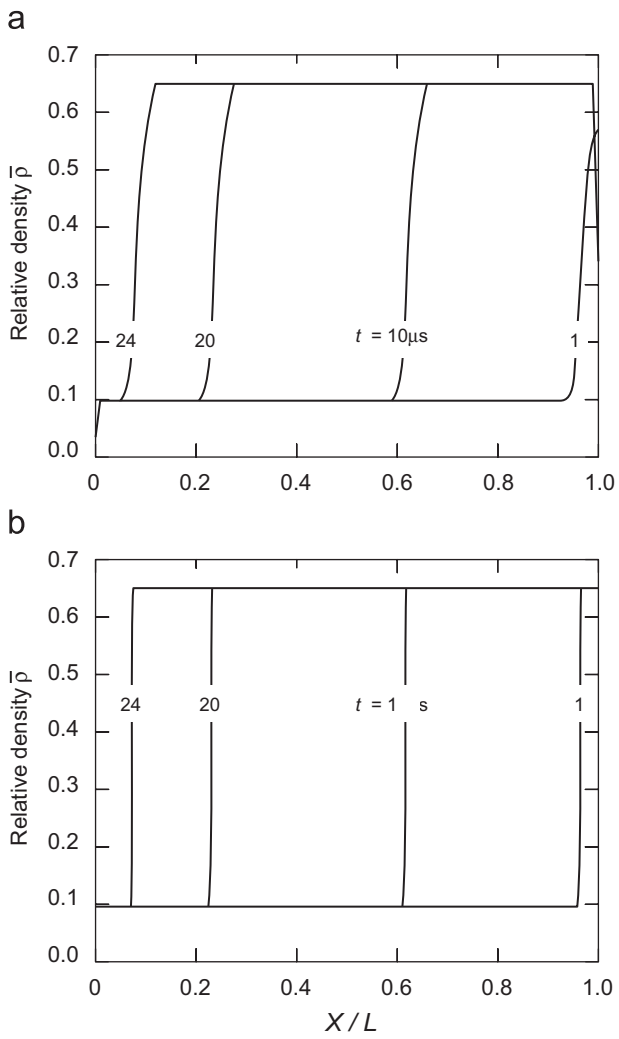

Fig. 8. Relative density $\bar{\rho}$ distributions in the $\bar{\rho}_{init} = 0.1$ sand slug at selected times after impact ($v_o = 1000\,\mathrm{m\,s^{-1}}$) for (a) $e = 0.9$ and (b) $e = 0.01$.

(the sand is reflected back and acquires a negative velocity); (iv) finally, the spallation front reaches the impacted surface, at $t \approx 22\,\mu s$, and the entire slug moves in a direction opposite to its initial velocity. The deformation of the sand is concentrated in a transition zone around the densification front. This zone is narrow for $e = 0.01$, with the transition from $v = v_o$ to $v = 0$ occurring over a length, $w \approx 0.01L$. The transition is more gradual when $e = 0.9$, with $w \approx 0.2L$. This shock width is strongly dependent on the choice of the function $f(e,\lambda)$ (Eq. (3.20))—discrete particle simulations of 1D impact would help identify the appropriate functional form. Informed by these mechanisms, we present an analytical estimate for the p_t history in Appendix C1. The viscous nature of the model in regime I (which results in a shock of finite width) stabilizes the numerical calculations and reduces instabilities typically associated with numerical calculations of strong shocks.

Influence of initial density. Here we contrast the impact of loose ($\bar{\rho}_{init} = 0.1$) and dense sand ($\bar{\rho}_{init} = 0.6$) against a stationary rigid target. All calculations are presented for a slug with mass/area, $m = 8\,\mathrm{kg\,m^{-2}}$ and co-efficient of restitution $e = 0.01$. The predictions of time variation of the pressure exerted by dense sand on the target are included in Fig. 9a for three selected values of the initial impact velocity v_o. A comparison with the corresponding loose-sand predictions (Fig. 6a) indicates that considerably higher pressures are exerted and that the pulse time is much shorter. The differences between the deformation mechanisms of the loose and dense sand are illustrated by examining the spatial velocity distributions, plotted in Fig. 9b for $v_o = 500\,\mathrm{m\,s^{-1}}$. The distributions are similar with two critical exceptions: (i) a sharp shock front forms in the loose sand, but is more diffuse in the dense sand and (ii) this weaker shock results in higher reflected velocities (approximately 80% of the impact velocity). These differences result in higher levels of momentum transfer to the target by the dense sand, as illustrated in Fig. 6b. While the loose-sand impacts are nearly plastic ($I_t/I_0 \approx 1$), irrespective of e, the dense-sand impacts are more elastic with I_t/I_0 approaching 1.8 increasing with decreasing e. These differences are

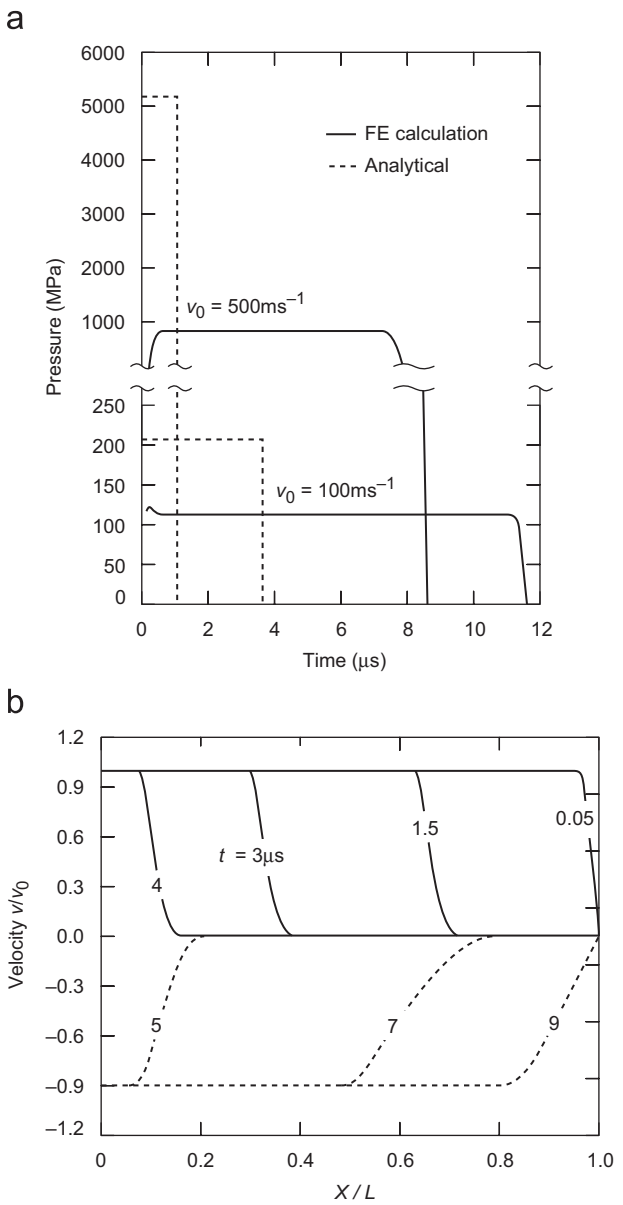

Fig. 9. (a) Finite-element predictions of the pressure versus time histories exerted by a dense-sand slug ($\bar{\rho}_{init} = 0.6$) on a stationary target. Results are shown for two selected values of the initial impact velocity v_o. (b) Normalised particle velocity distributions in the same sand slug at selected times after impact ($v_o = 500\,\mathrm{m\,s^{-1}}$). For comparison purposes we include analytical predictions of the pressure traces (Appendix C1) in (a).

rationalised by noting that the deformation of the loose sand is largely dissipative while the dense-sand behaviour has a large elastic densification component, which results in rebound and larger momentum transfer.

5. Spherical expansion of an aggregate shell

Explosions in air are much less damaging than shallow-buried explosives at the same stand-off. Moreover, mines buried in wet soil cause more damage than those in dry soil (Bergeron and Tremblay, 2000). In this section we summarise some experiments that illustrate these effects in a relatively simple geometric setting, in order to reveal the underlying physics as succinctly as possible. We explain these observations in terms of the constitutive model developed above and use comparisons between measurements and predictions as a preliminary step toward validation of the parameters chosen for the model.

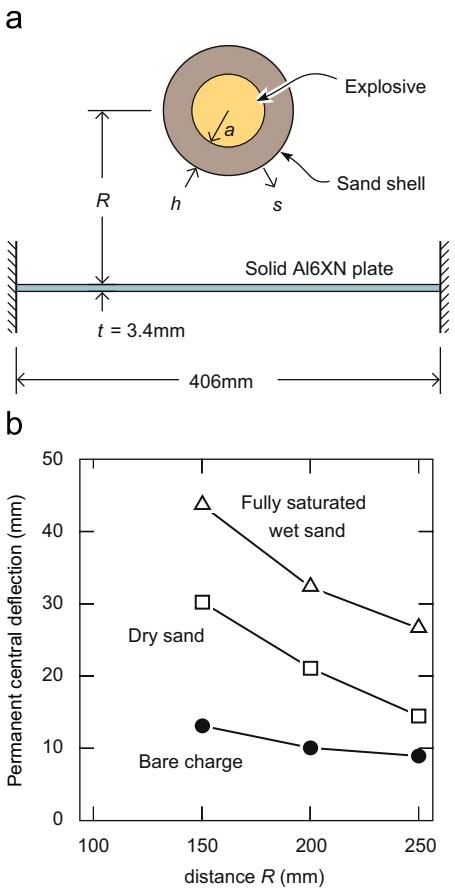

Fig. 10. (a) Sketch of the experimental setup in which a sphere of explosive surrounded by a shell of sand is detonated above a clamped square plate. (b) Measured permanent mid-span deflections as a function of the distance R. Results are shown for the explosive surrounded by dry sand, fully saturated sand, and the bare charge in air. Adapted from Dharmasena et al. (2009b).

5.1. Some key experimental findings

In order to quantify the differences in the dynamic response of structures to air blasts and soil ejecta, Dharmasena et al. (2009b) subjected steel plates to impact from the spherical expansion of a shell of granular material packed around a sphere of a high explosive (Fig. 10a). In these experiments, the sphere comprised 150 g of C4 (radius $a = 30$ mm) suspended at a distance (as measured from the centre of the charge; see Fig. 10a), $100 \leq R \leq 250$ mm from a square AL6XN steel plate of thickness $t = 3.14$ mm. The plate, of side $L = 406$ mm, was fully clamped along all four edges. Three types of experiment were conducted:

(i) *bare charge* wherein the C4 ball was detonated in air;
(ii) *dry sand* in which the C4 ball was surrounded by an $h = 46.2$ mm thick shell of aggregate comprising 60% by volume of spherical glass micro-spheres (diameter $D = 200\,\mu$m);
(iii) *wet sand* wherein the ball was surrounded by the same thickness of water-saturated aggregate comprising the same glass micro-spheres, but with the void space filled with water.

The permanent maximum deflections (at the mid-span of the plate) are plotted in Fig. 10b as a function of the stand-off. The measurements reveal that the deflections decrease in the following order: wet sand → dry sand → bare charge. Visual indications from high-speed photographs reveal that the rates of expansion of both the dry (Fig. 11a) and wet (Fig. 11b) sand shells are approximately equal. However, the explosive gases are clearly visible over the entire surface of the expanded dry sand shell whereas for wet sand they vent from around the wire used to suspend the sphere. For the dry sand, the aggregate has become a loose spray, permitting light to pass through to the interior, where the explosive gases are present. By contrast, the expanded shell of the water-saturated aggregate appears to be solid and opaque (clumped together).

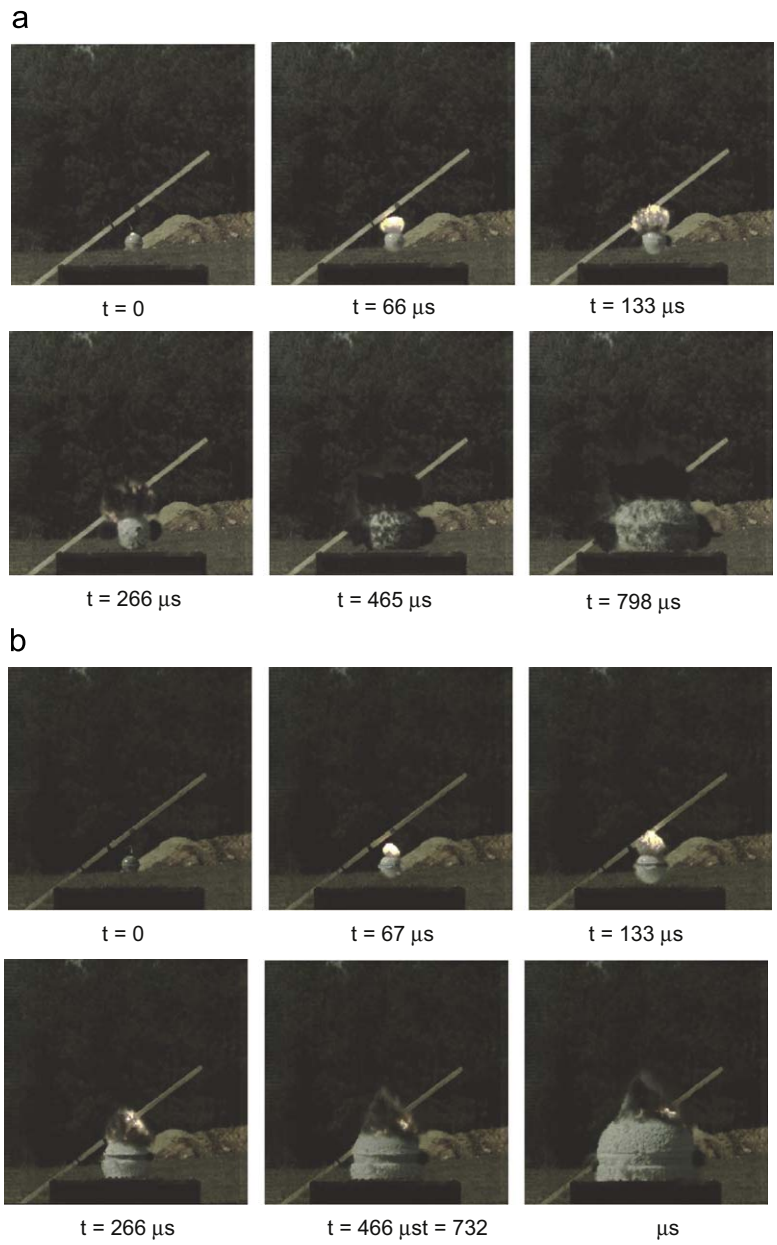

Fig. 11. High-speed photographs of the expansion of the spherical shells of (a) dry and (b) wet sand. Time $t = 0$ corresponds to the instant of detonation. Adapted from Dharmasena et al. (2009b).

5.2. *Model predictions: wet and dry sand*

We employ the foregoing sand constitutive model to develop an understanding of these observations, using a finite-deformation Lagrangian finite-element scheme. As a reference case we consider a 0.454 kg sphere of TNT surrounded by an $h = 12$ cm thick shell of wet or dry sand. One-dimensional constant strain, spherically symmetric elements were employed with 100 and 400 elements used to model the TNT and aggregate shell, respectively. The interface between the TNT and aggregate was modelled using a penalty contact algorithm such that it could transmit compressive (but not tensile) radial stresses. The surrounding air was not explicitly modelled since the aggregate particles flow through the surrounding air at high speed. The solid TNT has a density 1600 kg m^{-3} so that the un-deformed explosive sphere has radius 4.1 cm. Following Brode (1955) we initialize the explosive product variables in the volume it originally occupied as a region of uniform pressure and zero initial velocity. These detonation products are modelled as an ideal gas with an equation of state for

the pressure:

$$p = \rho_e(\gamma - 1)E - p_a, \tag{5.1}$$

where $\gamma = 1.4$ is the ratio of the specific heat capacities, ρ_e the current density, E the specific energy per unit mass, and $p_a = 0.1$ MPa the ambient atmospheric pressure; i.e. we do not account for the surrounding air explicitly but rather model the effect of atmospheric pressure by reducing the effective pressure of the detonation products.[1] Assuming an adiabatic process, the evolution of the specific energy is governed by the relation

$$\dot{E} = (1 - \gamma)E\dot{\varepsilon}_{kk}, \tag{5.2}$$

where $\dot{\varepsilon}_{kk}$ is the volumetric strain rate. In order to stabilize the numerical calculations and capture possible shocks, we employ both linear and quadratic artificial viscosities as proposed by von Neumann and Richtmyer (1950) and described in detail in Kambouchev et al. (2006). The detonation occurs at time $t = 0$—at this instant, the specific energy and density have values $E = 4.2\,\mathrm{MJ\,kg^{-1}}$ and $\rho_e = 1600\,\mathrm{kg\,m^{-3}}$.

The aggregate shell was modelled using the following material parameters: particle diameter $D = 200\,\mu\mathrm{m}$, $\rho = 2700\mathrm{kg\,m^{-3}}$, co-efficient of restitution $e = 0.9$ (representative for silica and glass; Bowden and Tabor, 1986), and initial and critical volume fractions $\bar{\rho}_{crit} = \bar{\rho}_{init} = 0.6$ corresponding to the dense random packing density of mono-sized spheres. The Bagnold parameters are unchanged at $\alpha = 0.1$, $\beta = 0.3$. The initial smeared-out densities of the dry and fully saturated wet sand were $\rho_s = \bar{\rho}_{init}\rho = 1620\,\mathrm{kg\,m^{-3}}$ and $\rho_s = \bar{\rho}_{init}\rho + (1 - \bar{\rho}_{init})\rho_w = 2020\,\mathrm{kg\,m^{-3}}$, respectively, where $\rho_w = 1000\,\mathrm{kg\,m^{-3}}$ is the density of water. Based on the p-wave wave speed in wet sand, $c_p \approx 2250\,\mathrm{m\,s^{-1}}$ (Press, 1966), we choose $\kappa = 10.7$ GPa for wet sand, whereas $\kappa = 1.7$ GPa for dry sand (see Section 4).

The predictions are included in Fig. 12. In these figures the radial positions of three separate fronts (the outer radius of the TNT gases, the trailing edge of the sand, and the leading edge of the sand), as measured from the centre of the TNT sphere, are plotted as functions of time, with $t = 0$ defined as the instant of detonation. *Dry sand*: detonation results in the expansion of the high-pressure TNT gases, which induce a compression wave in the shell. While the trailing edge of the sand starts moving with the gases, the leading edge remains stationary until the compression wave arrives at time $t = 110\,\mu\mathrm{s}$. This compression wave is reflected as a tensile wave, resulting in the outward motion of the leading edge at radial velocity greater than that of the trailing edge, causing an increase of the aggregate shell thickness. *The density of the sand within this shell thus decreases significantly.* At $t = 1.5$ ms the pressure within the expanding TNT gases has reduced sufficiently that atmospheric pressure now starts to re-compress the explosive products and the gas bubble slowly starts to collapse. Recall that the interface between the gases and the sand can sustain only compressive radial stresses. Thus, the trailing edge of the sand separates from the gases and continues to move radially outward. *Wet sand* (Fig. 12b): Given the higher c_p, the compressive stress wave reaches the outer surface of the shell almost instantaneously. Subsequently, unlike in the dry sand, the trailing and leading edges almost converge. Recall that the spherical expansion of the shell has the tendency to reduce the density of the sand. However, the radial contraction compensates for the spherical expansion, resulting in an almost constant sand density. This clumping *is not related to the cohesive stresses in the wet sand* (which are typically only of the order of 0.2 MPa and neglected in this analysis). Rather, it is an inertial effect that can be explained as follows. The high bulk modulus for the wet sand implies that the elastic energy it stores is about 10 times smaller than that in the dry sand. Thus, there is less energy available for the high-velocity spallation, enabling the leading and trailing edges of the shell to converge (Fig. 12b).

In order quantify the loading of structures by the ejected sand, we consider the static and stagnation pressures given by

$$p_s = -\sigma_{kk}/3 \tag{5.3}$$

and

$$p_d = p_s + \rho_c v^2, \tag{5.4}$$

respectively, where $\rho_c \equiv \bar{\rho}\rho$ is the current density of the sand and v its radial velocity. These pressures are measured at a radial stand-off s from the surface of the un-deformed sand shell with σ_{ij} in (5.3) being the material stresses. The predicted temporal variations of p_d and p_s for the wet sand are plotted in Figs. 13a and b, respectively, at a stand-off, $s = 0.1$ m (as measured from the surface of the sand shell; see Fig. 10a). The sand first reaches this location at time $t = 0.52$ ms after the detonation, resulting in a pressure pulse of duration ≈ 0.1 ms.[2] The peak stagnation pressure of 200 MPa is significantly higher than the static pressure of 12 MPa, suggesting that the primary loading may be attributed to the kinetic energy of the sand. Recall that the radial velocity and density of wet sand remain almost constant as the sand shell expands. Given that the major contribution to p_d is from the $\rho_c v^2$ term (5.4), we anticipate that the peak dynamic pressure will be un-affected by stand-off. This is confirmed in Fig. 13c, wherein the temporal variation of p_d is plotted for a larger stand-off, $s = 0.9$ m. The major difference between Figs. 13a and c is the duration of the pulse, which decreases with increasing s due

[1] Just after denotation, the pressure of the TNT gases is a few GPa and the p_a term in Eq. (5.1) has a negligible effect. This term starts to play a significant role only once the pressure within the expanded detonation products has dropped to near atmospheric pressure.

[2] The long tail in the p_s trace ($t \geq 0.6$ ms) is due to the TNT gases reaching the measurement location.

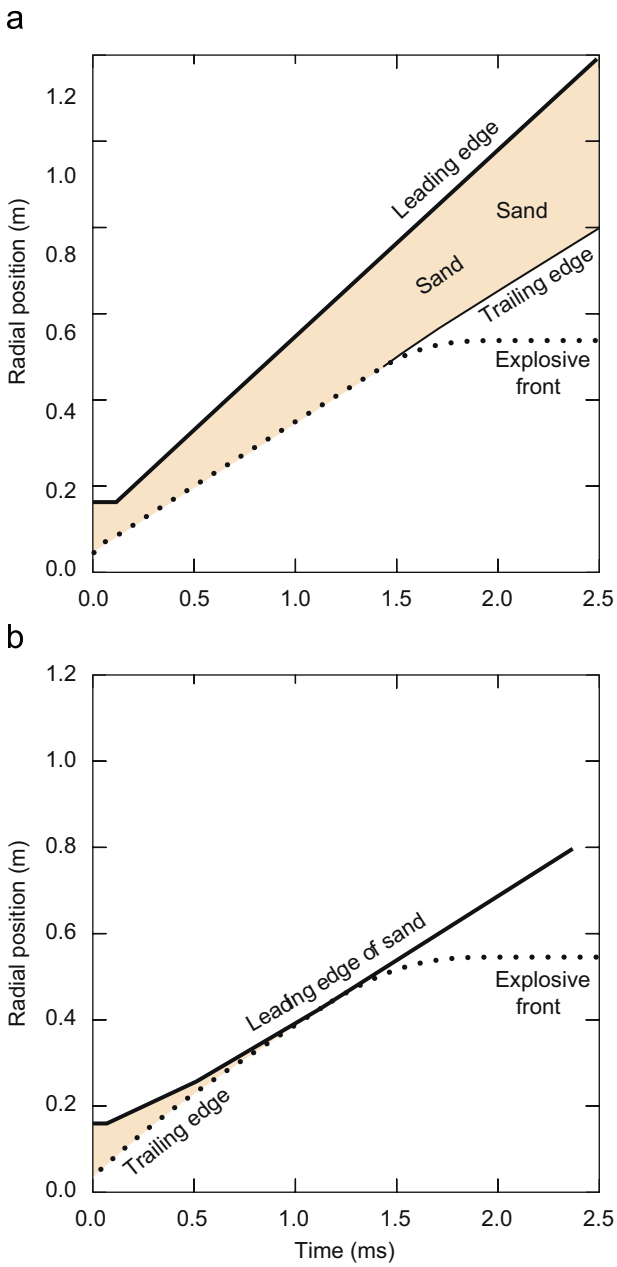

Fig. 12. Finite-element predictions of the time evolution of the radial positions of the leading, trailing, and explosive gas fronts for an $h = 12$ cm shell of (a) dry and (b) wet sand surrounding a 0.454 kg sphere of TNT. Time $t = 0$ corresponds to the instant of detonation.

to the thinning of the expanding shell (see Fig. 12b). We contrast these findings with the corresponding predictions of p_d for dry sand (Fig. 14) for stand-offs $s = 0.1$ and 0.9 m. Three main differences are observed:

(i) The durations of the pressure pulses for the dry sand are significantly longer and increase (rather than decrease) with increasing stand-off.
(ii) The increase in the pulse duration implies that the sand becomes more dispersed with increasing s, resulting in a decrease in ρ_c. Given that the major contribution to p_d is from the $\rho_c v^2$, the peak stagnation pressure drops significantly with increasing stand-off.
(iii) The sand segregates toward the leading and trailing edges of the expanding dry sand shell, resulting in higher values of p_d near those edges.

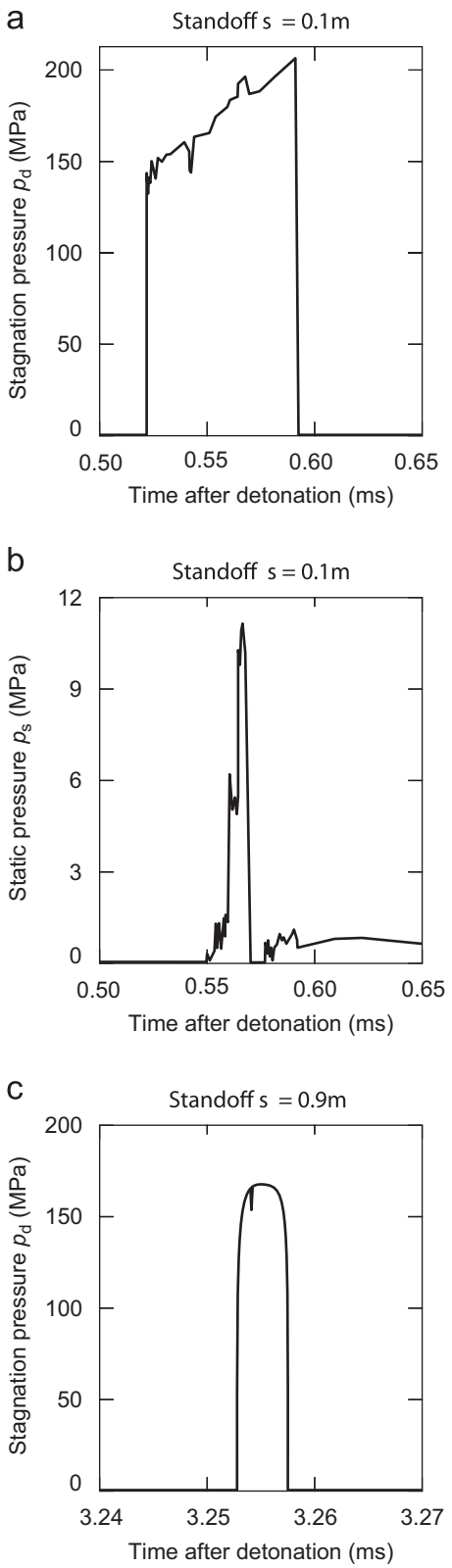

Fig. 13. Predictions of the time traces of the (a) stagnation pressure p_d and (b) static pressure p_s due to the wet sand explosion at a stand-off, $s = 0.1$ m. The corresponding p_d trace at $s = 0.9$ m is included in (c). The explosive comprised a 0.454 kg sphere of TNT surrounded by an $h = 12$ cm shell of wet sand. The stand-off s was measured from the surface of the un-deformed shell of the wet sand (Fig. 10a).

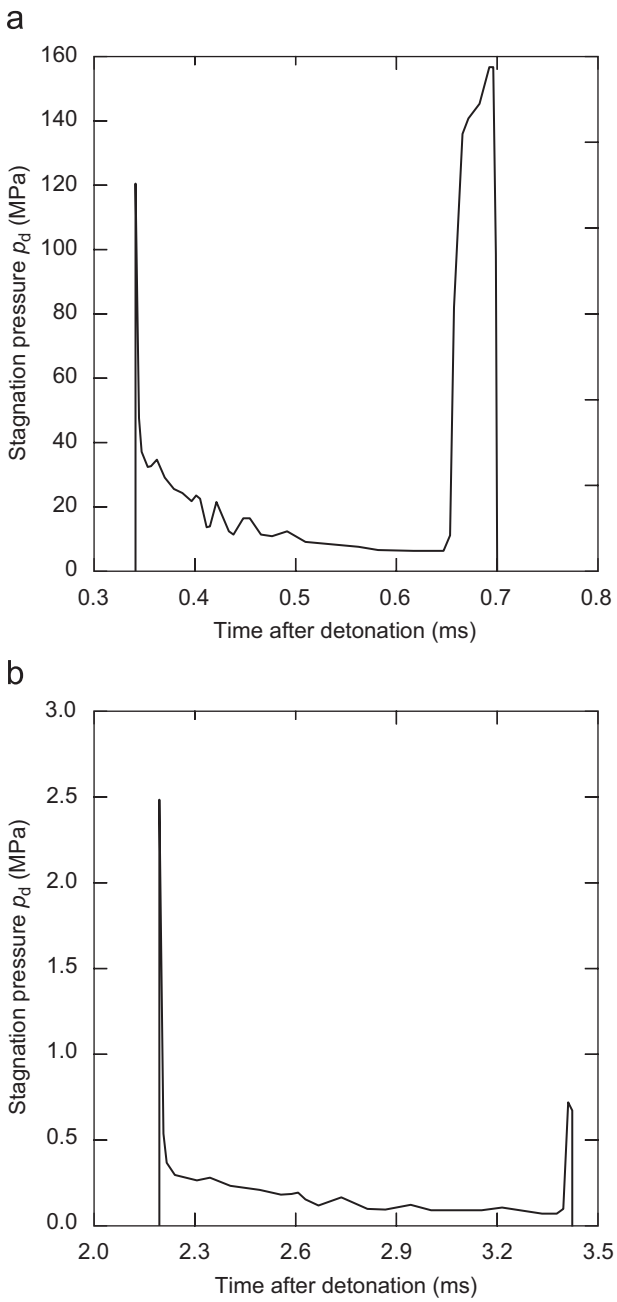

Fig. 14. Predictions of the time traces of the stagnation pressure p_d due to the dry sand explosion at a stand-off (a) $s = 0.1$ m and (b) $s = 0.9$ m. The explosive comprised a 0.454 kg sphere of TNT surrounded by an $h = 12$ cm shell of dry sand.

By defining the impulse

$$I_s = \int_{t_a}^{t_e} p_d dt, \tag{5.5}$$

where t_a and t_e are the times of arrival of the leading and trailing edges, respectively, of the sand shell at the measurement location (i.e. the effect of the TNT gases is neglected in this definition[3]), the average pressure at this

[3] For stand-offs in the range, $s \geq 0.1$ m, the additional momentum due to the explosive products is negligible compared with the momentum of the sand. Recall that the pressure tail at $t \geq 0.6$ ms in Fig. 13b is due to the explosive gases. This tail has a negligible effect on the $p_d(t)$ trace in Fig. 13a.

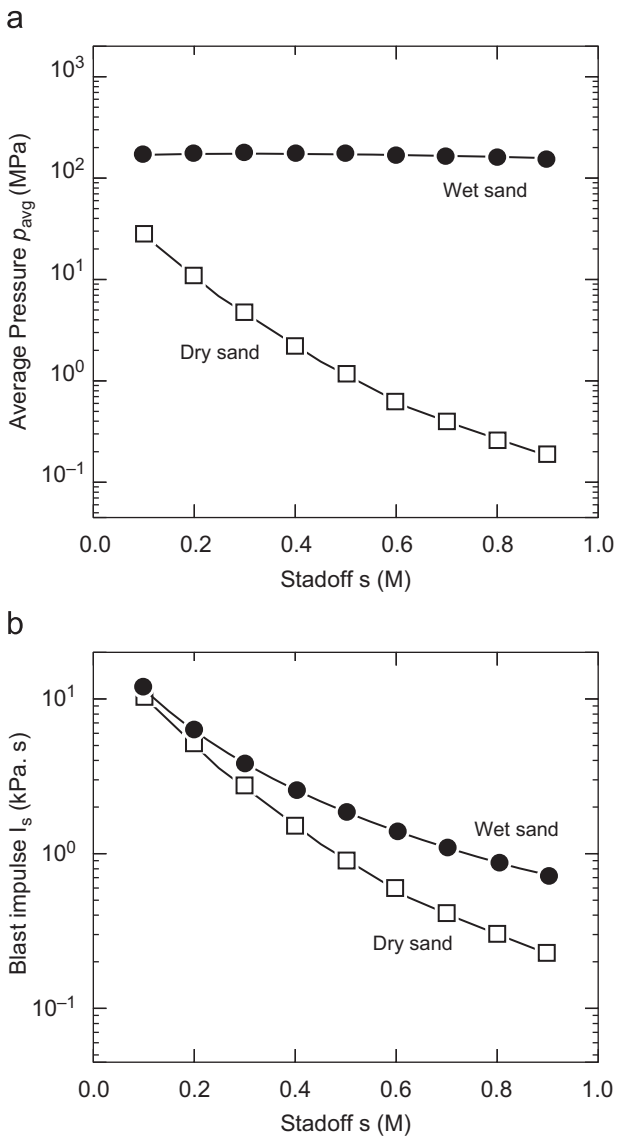

Fig. 15. Predictions of the variation of (a) the average pressure p_{avg} and (b) impulse I_s with stand-off s for dry and wet sand explosions. The explosive comprised a 0.454 kg sphere of TNT surrounded by an $h = 12$ cm shell of sand.

location becomes

$$p_{avg} = \frac{I_s}{t_e - t_a}. \tag{5.6}$$

The pressure p_{avg} and impulse I_s are plotted in Figs. 15a and b, respectively, for dry sand and wet sand as a function of the stand-off s. The differences between the two cases are summarised as follows:

(i) the pressures p_{avg} associated with the wet sand explosion are significantly higher and decrease very gradually with increasing s compared to the dry sand explosion and
(ii) the impulses due to the wet sand explosion are also slightly higher.

The spherical expansion of the shell implies that the impulse should always decrease as $1/s^2$. We conclude that the higher deflections of the plate in the wet sand explosions are due to a combination of the higher impulse and pressure; albeit full sand–structure interaction calculations (Dharmasena et al., 2009b) are required for a comprehensive interpretation.

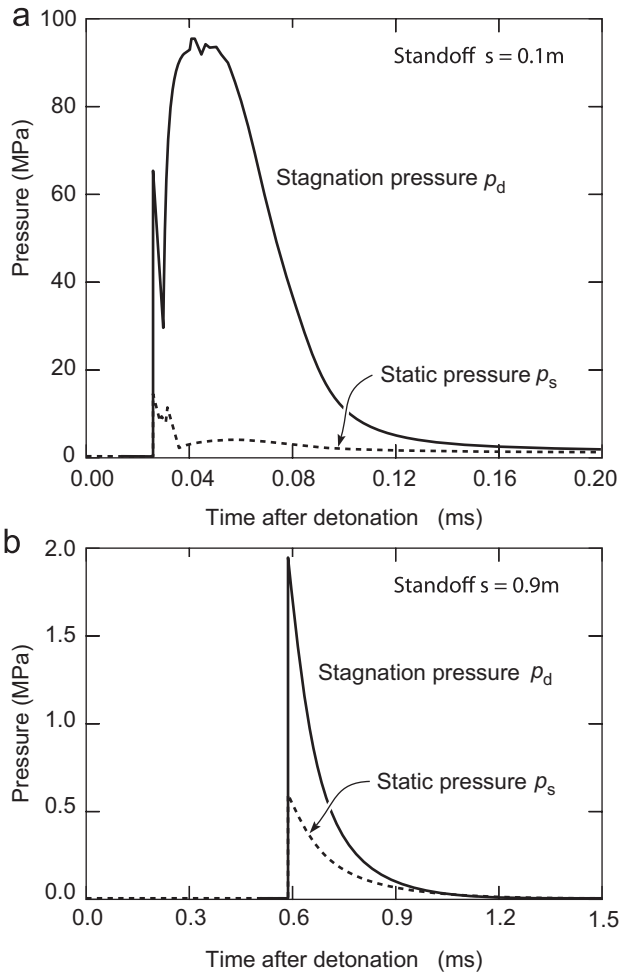

Fig. 16. Predictions of the time traces of the stagnation pressure p_d and static pressure p_s due to the explosion of a 0.454 kg sphere of TNT in air. The pressures are plotted for stand-offs (a) $s = 0.1$ m and (b) $s = 0.9$ m.

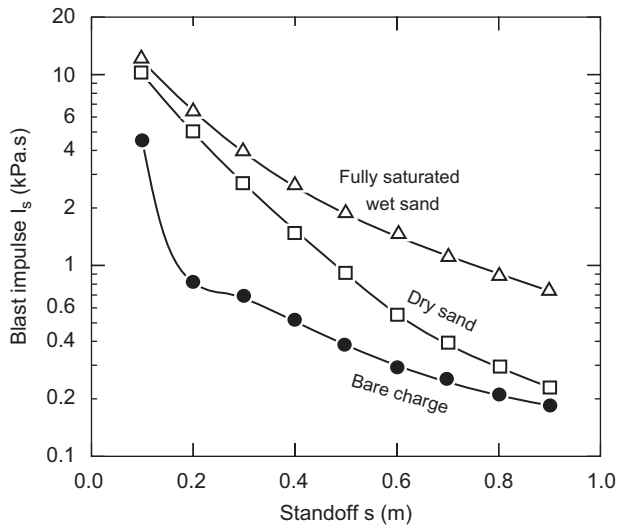

Fig. 17. Predictions of the blast impulse I_s as a function of stand-off s for the explosion of a 0.454 kg sphere of TNT in air (bare charge); or surrounded by $h = 12$ cm shells of dry sand or fully saturated wet sand.

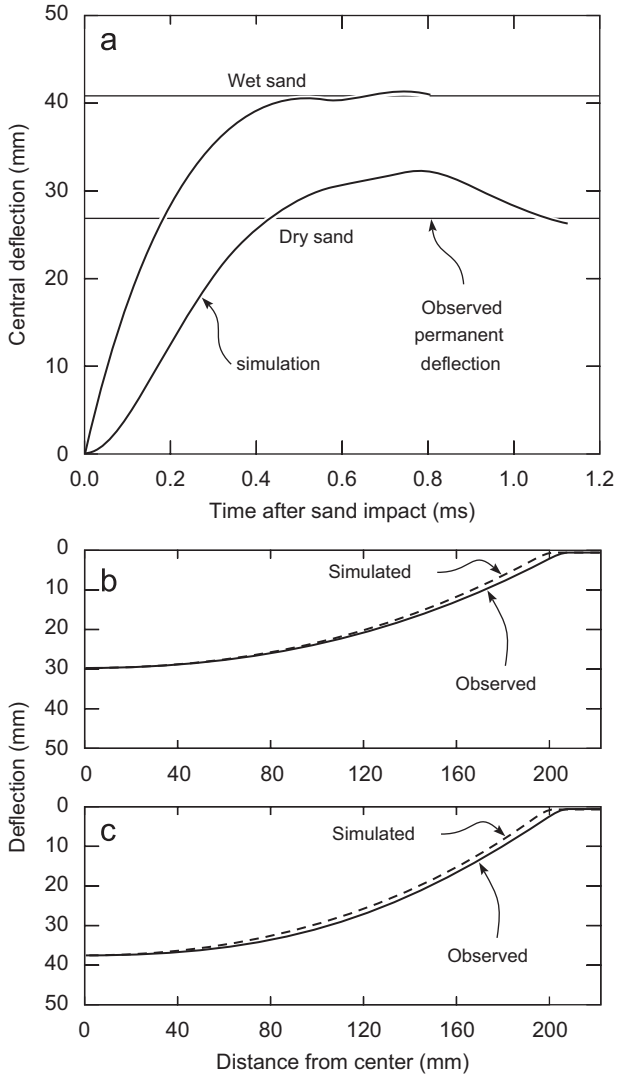

Fig. 18. Comparisons between measurements and predictions of plate deflections due to the impact of a spherically expanding wet and dry sand shell at a distance $R = 200$ mm (from Dharmasena et al., 2009b). (a) Predictions of the deflection time histories of the plate mid-span. The measured final deflections are also included. Comparison between the measured and predicted final deflected profiles of the plates impacted by (b) dry and (c) wet sand.

5.3. Comparison with air blasts

The experiments conducted by Dharmasena et al. (2009b) suggest that blasts involving sand (wet or dry) cause significantly larger deformations than air blasts. To quantify the effect we performed calculations identical to those reported above, but with air surrounding the C4 sphere. The calculations were performed using 1D spherically symmetric finite elements with no mixing of the TNT gases with air. The calculations were terminated before the air shock reached the outer edge of the finite-element mesh to prevent any spurious reflections. The atmospheric air was modelled using the adiabatic ideal gas relations—Eqs. (5.1) and (5.2) with $\gamma = 1.4$ and $p_a = 0$. In its initial state, air was assumed to be stationary and at a temperature $T = 20\,^{\circ}\mathrm{C}$ with an initial density $\rho_e = 1.19\,\mathrm{kg\,m^{-3}}$ and specific energy $E = 210\,\mathrm{kJ\,kg^{-1}}$. Predictions of the temporal variations of the static and stagnation air pressures at stand-offs $s = 0.1$ and 0.9 m are included in Fig. 16 with $t = 0$ corresponding to the instant of detonation. The static pressures, pulse durations, and free-field impulses (defined as the area under the $p_s(t)$ curves) agree well with the standard nomo-graphs (Kingery and Bulmash, 1984; US Army Technical Manual, 1992) confirming the accuracy of the method.

The results in Fig. 16 indicate that, similar to sand explosions, the stagnation pressures for air blasts are significantly higher than the corresponding static pressures. Thus, we compare the air and sand blast loadings on the basis of their stagnation pressure impulses as defined by Eq. (5.5) for the sand blasts and

$$I_s = \int_{t_a}^{\infty} p_d \, dt \tag{5.7}$$

for air blasts (where t_a is the time of arrival of the air shock at the measurement location). These predictions of I_s are included in Fig. 17 as a function of the stand-off s for the three cases. Clearly, the impulses I_s for a given stand-off are in the decreasing order: wet sand → dry sand → bare charge, identical to the ordering of the plate deflections (Fig. 10b). Thus, bare charge blasts are less efficient at converting the energy of the explosive to kinetic energy of the plate for the following reasons. The sand first compresses by mainly elastic deformation and then expands due to both the release of the stored energy and the push by the high-pressure detonation products. The dissipation in this process is relatively small, resulting in conversion of most of the explosive energy to kinetic energy of the sand. The explosion in air results in the formation of a compressive shock wave with consequent entropy production across the shock, as quantified by the Rankine–Hugoniot jump conditions (Liepmann and Roshko, 2001). This entropy production reduces the energy available to do usable external work.

5.4. Future perspectives and experimental comparisons

The foregoing sand model was employed by Dharmasena et al. (2009b) in a coupled Eulerian/Lagrangian simulation setup to predict the plate deflections measured in the experiments described in Section 5.1. The predictions of temporal variations of deflections of the plate mid-span are sketched in Fig. 18a for the wet and dry sand cases corresponding to $R = 200$ mm. The measured permanent deflections are also included Fig. 18a, while the measured and predicted deflected profiles of the plates impacted by dry and wet sand are compared in Figs. 18b and c, respectively. Good agreement between the measurements and predictions is observed, including the increased plate deflections in the wet sand explosions. The slight discrepancies near the clamped supports are attributed to the fact that while perfect clamping was assumed in the calculations, some slippage of the plates within the supports occurred in the experiments. Readers are referred to Dharmasena et al. (2009a, b) for further details of the calculations, a detailed interpretation of the results, and further validations of the foregoing sand model.

6. Concluding remarks

A constitutive model is developed for the high-rate deformation of an aggregate of mono-sized spherical particles. It spans two regimes. *Regime I:* when the aggregate particles are widely dispersed, the contacts between the particles entail collisions. This behaviour is modelled by extending an existing analysis (Bagnold, 1954) to include combinations of shear and volumetric deformations. Inclusion of this regime is essential for cases where the soil disperses and forms ejecta. *Regime II*: at high packing densities, the contacts between particles are semi-permanent, enabling existing soil mechanics models (such as the Drucker–Prager model) to be used. This regime addresses the response when the soil impacts a target. In order to explore the utility of the new model for probing dynamic soil–structure interactions in landmine explosions, two example problems have been investigated.

In the first, the dynamic loading of a stationary target by the 1D impact of a sand slug onto a rigid target is investigated with the objective of exploring the roles of the co-efficient of restitution, e, and the incoming sand density. The simulations reveal that, when the sand compacts against the target, a shock front forms, which separates the densified and loose zones. The width of this shock increases as the particle collisions become more elastic (with increasing co-efficient of restitution). But, unlike single-particle impacts, *the momentum transmitted to the target is insensitive to e.* Conversely, the pressure induced and the momentum transmitted to the target increase dramatically upon increasing the initial density of the incoming sand.

Second, the explosive spherical expansion of shells of dry and fully saturated wet sand has been modelled. Consistent with experimental measurements, the calculations predict that wet sand clumps together while dry sand disperses. Moreover, this clumping is not related to the cohesive strength of the wet sand but a result of its high initial bulk modulus. The clumping results in higher stagnation pressures and larger impulses for wet sand blasts compared with dry. In turn, both are more severe than air blasts. Future investigations will employ this constitutive model to investigate the sand–structure interactions in a fully coupled manner using coupled Eulerian/Lagrangian finite-element formulations.

Acknowledgements

Support from the Office of Naval Research through a Multidisciplinary University Research Initiative program on "Cellular materials concepts for force protection", Prime Award no. N00014-07-1-0764 is gratefully acknowledged. The program manager was Dr David Shifler.

Appendix A1. The effect of grain temperature

Consider the deformation of a loose aggregate of spherical particles of diameter D and solid density ρ. The Bagnold (1954) analysis suggests that the stresses scale with the square of the applied mean strain rate and thus requires the stresses to vanish at locations where the mean strain rates are zero. However, at these locations, particle interactions may

still persist as enduring contact forces between particles or as impulsive forces in collisions resulting from the fluctuations of the particle velocity about the mean. The energy corresponding to these fluctuations will be ultimately converted to thermal energy via inelastic collisions. Thus, the Bagnold-type analysis, which neglects such effects, is appropriate when the relaxation time associated with this decay is small compared to other relevant time scales in the problem.

Here we present an approximate calculation of the relaxation time of the stresses in order to gauge the applicability of the model for understanding granular impacts. Define $\tilde{v}$ as representative of the magnitude of the fluctuation velocities of the particles. The grain temperature T is then by defined as $T \equiv \tilde{v}^2$ (Jenkins and Savage, 1983). The loss in fluctuation energy per collision is given as

$$\Delta\tilde{E} = \frac{\pi}{12} D^3 \rho T (1 - e^2), \tag{A.1}$$

where e is the co-efficient of restitution between the particles. Given an average grain spacing ℓ, the number of collisions per unit time is $\sqrt{T}/\ell$ and the dissipation rate per unit volume follows as

$$\Delta\tilde{E}_v \approx \frac{\pi}{6} \frac{D^3}{\ell^4} \rho T^{3/2} (1 - e^2). \tag{A.2}$$

The fluctuation energy per unit volume is defined as $\pi/6(D/\ell)^3 \rho T$. Equating the rate of change of this energy to $\Delta\tilde{E}_v$ we obtain

$$\frac{\pi}{6} \left(\frac{D}{\ell}\right)^3 \rho \dot{T} = -\frac{\pi}{12} \frac{D^3}{\ell^4} \rho T^{3/2} (1 - e^2). \tag{A.3}$$

We define the relaxation time t_c as the time for an initial temperature T_0 to decay to $T = c^2 T_0$ (where $c < 1$). Solving the first-order differential equation (A.3) we obtain t_c as

$$t_c = \frac{D(1 - c)}{\bar{\rho}^{1/3} c (1 - e^2) \sqrt{T_0}}, \tag{A.4}$$

where we have used the scaling that the relative density of the aggregate $\bar{\rho} \approx (D/\ell)^3$.

The time scale relevant to the applied loading is given as $1/\dot{\varepsilon}_{ref}$, where $\dot{\varepsilon}_{ref}$ is a representative applied strain rate. We then define the ratio of the relaxation time t_c to the loading time as

$$\eta \equiv \frac{D(1 - c)\dot{\varepsilon}_{ref}}{\bar{\rho}^{1/3} c (1 - e^2) \sqrt{T_0}}. \tag{A.5}$$

Based on the above discussion, the Bagnold-type analysis, which neglects the effects of grain temperature, is valid in the limit $\eta \ll 1$.

We proceed to gauge the validity of the model for sand impact problems similar to that analysed in Section 4. Representative parameters for this situation are $D = 200\,\mu\text{m}$, $\bar{\rho} = 0.1$, $e = 0.9$, $c = 0.3$ (i.e. the decay time t_c corresponds to a final temperature $T = 0.1T_0$) and a representative strain rate $\dot{\varepsilon}_{ref} = v_o/L$, where v_o is the impact velocity and L the length of the impacting sand slug. In this impact situation the stresses generated by random motion of the particles are significant only when the fluctuation velocities are of the order of the impact velocity. We thus choose $\sqrt{T_0} = v_o$. Substituting these values into Eq. (A.5) gives $\eta = 0.02$ for the choice $L = 0.1$ m. This suggests that the relaxation time associated with the decay of the fluctuation energy is much smaller than the representative loading time and provides a justification for neglecting effects of grain temperature in analysing the loading of structures by high-velocity sand sprays.

Appendix B1. A visco-plastic Drucker–Prager model

In this study the consolidation stresses σ^c_{ij} are assumed to be purely elastic with a finite bulk modulus and a zero shear modulus. However, in general these consolidation stresses would be specified via an appropriate soil mechanics model such as Cam–Clay, Mohr–Coulomb, or Drucker–Prager. As an example here we detail the specification of σ^c_{ij} via a visco-plastic Drucker–Prager-type model.

The total strain rate $\dot{\varepsilon}_{ij}$ of the consolidating soil is given by the sum

$$\dot{\varepsilon}_{ij} = \dot{\varepsilon}^e_{ij} + \dot{\varepsilon}^p_{ij}, \tag{B.1}$$

where $\dot{\varepsilon}^e_{ij}$ and $\dot{\varepsilon}^p_{ij}$ are the elastic and plastic strain rates, respectively. Assuming an isotropic elastic response, the elastic strain rate follows as

$$\dot{\varepsilon}^e_{ij} = \frac{1 + \nu}{E} \dot{\sigma}^c_{ij} - \frac{\nu}{E} \dot{\sigma}^c_{kk} \delta_{ij}, \tag{B.2}$$

where E and ν are the Young's modulus and elastic Poisson's ratio, respectively. The plastic strain rates are specified via a rate-dependent associated flow version of a Drucker–Prager-type model (with no compressive cap). We define a

flow potential

$$\Phi \equiv \frac{\dot{\varepsilon}_o \sigma_o}{m+1}\left(\frac{\hat{\sigma}}{\sigma_o}\right)^{m+1}, \tag{B.3}$$

where $\dot{\varepsilon}_o$ is a reference strain rate, m the strain rate sensitivity exponent, and σ_o the uniaxial compressive yield strength with the effective stress $\hat{\sigma}$ defined as

$$\hat{\sigma} \equiv \begin{cases} \dfrac{\sigma_e^c + \vartheta \sigma_m^c}{1 - \vartheta/3} & \text{if } \sigma_e^c > -\vartheta \sigma_m^c \\ 0 & \text{otherwise} \end{cases}. \tag{B.4}$$

Here the mean stress $\sigma_m^c = \sigma_{kk}^c/3$, the von-Mises effective stress $\sigma_e^c = \sqrt{(3/2) S_{ij}^c S_{ij}^c}$, where $S_{ij}^c \equiv \sigma_{ij}^c - \delta_{ij}\sigma_m^c$ and ϑ is a material constant related to the friction angle of the soil. Assuming associated flow, the plastic strain rate follows from this flow potential as

$$\dot{\varepsilon}_{ij}^p = \frac{\partial \Phi}{\partial \sigma_{ij}^c}. \tag{B.5}$$

For a given strain rate $\dot{\varepsilon}_{ij}$, Eqs. (B.1)–(B.5) can be solved to calculate the consolidation stresses σ_{ij}^c. We note that for large values of the exponent m, the model reduces to an approximately rate-independent associated flow version of the Drucker–Prager model.

Appendix C1. An analytical model for sand slug impact

The 1D compression of sand can be modelled by the Hugoniot illustrated in Fig. C1a, wherein the sand supports no stress in its loose state and locks up at a strain ε_D to become a rigid solid with relative density $\bar{\rho}_{crit}$. The densification front starts at the impacted end and travels with a shock wave velocity c_p toward the distal end (Fig. C1b). Upstream of the shock the sand has a velocity v_o and relative density $\bar{\rho}_{init}$ while downstream it is densified with a relative density $\bar{\rho}_{crit}$, and stationary ($v = 0$). At any instant the sand is non-deforming except for a jump in compressive strain, $\varepsilon_D = 1 - \bar{\rho}_{init}/\bar{\rho}_{crit}$, across the shock. With a stress $\sigma = 0$ upstream from the shock, conservation of momentum implies that the compressive stress in the densified stationary region is

$$p_t = \rho \bar{\rho}_{init} c_p v_o. \tag{C.1}$$

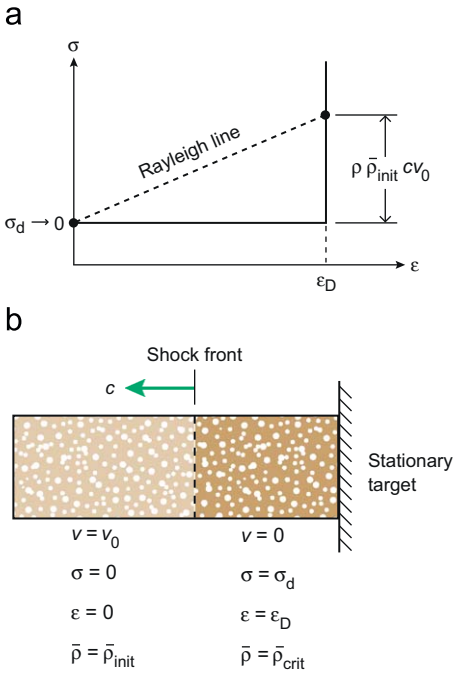

Fig. C1. (a) Idealised quasi-static uniaxial stress versus strain response of low-density sand. (b) Sketch of the propagation of a one-dimensional shock wave in a sand slug impacting a stationary target.

This stress equals the pressure exerted by the sand on the target. Mass conservation across the shock provides

$$c_p = \frac{v_o}{\varepsilon_D}, \tag{C.2}$$

and thus the pressure exerted on the target becomes

$$p_t = \rho \bar{\rho}_{init} \frac{v_o^2}{1 - \bar{\rho}_{init}/\bar{\rho}_{crit}}. \tag{C.3}$$

The shock reaches the distal end at time L/c_p and therefore the rectangular pressure pulse has duration

$$t_{pulse} = \frac{m(1 - \bar{\rho}_{init}/\bar{\rho}_{crit})}{v_o \rho \bar{\rho}_{init}}. \tag{C.4}$$

The analytical predictions of the pressure pulse histories are included in Fig. 6a and agree well with the FE simulations that employ the full constitutive model. Note that the elastic deformations of the sand beyond the critical relative density $\bar{\rho}_{crit}$ are neglected in this model, with all of the kinetic energy of the sand slug dissipated within the shock front. Thus, the analytical model predicts a perfectly plastic impact in all cases, with $I_t = I_o$. Given these considerations, the model is accurate only for low initial densities, $\bar{\rho}_{init} \ll \bar{\rho}_{crit}$. Indeed, attempts to use the model for high initial densities have revealed its inadequacy as seen in Fig. 9a.

References

Bangash, M.Y.H., 1993. Impact and Explosion—Analysis and Design. CRC Press, Boca Raton, FL, USA.

Bagnold, R.A., 1954. Experiments on a gravity-free dispersion of large solid particles in a Newtonian fluid under shear. Proceedings of the Royal Society of London A 225, 49–63.

Bathurst, R.J., Rothenburg, L., 1988. Micromechanical aspects of isotropic granular assemblies with linear contact interactions. Journal of Applied Mechanics, ASME 55, 17–23.

Bergeron, D., Walker, R., Coffey, C., 1998. Detonation of 100-gram anti-personnel mine surrogate charges in sand-A test case for computer code validation. Suffield Report No. 668, Defence Research Establishment Suffield, Ralston, Alberta, Canada.

Bergeron, D., Tremblay, J.E., 2000. Canadian research to characterize mine blast output. In: Proceedings of the 16th International MABS Symposium, Oxford, UK.

Bowden, F.P., Tabor, D., 1986. The Friction and Lubrication of Solids, second ed. Clarendon Press, Oxford, UK.

Braid, M.P., 2001. Experimental Investigation and Analysis of the Effects of Anti-Personnel Landmine Blasts. Defence Research Establishment Suffield, Canada (Special Publication, DRES SSSP 2001-188).

Brode, H.L., 1955. Numerical solutions of spherical blast waves. Journal of Applied Physics 26, 766–775.

Campbell, C.S., Brennen, C.E., 1985. Chute flows of granular material: some computer simulations. Journal of Applied Mechanics, ASME 52, 172–178.

Campbell, C.S., 2002. Granular shear flows at the elastic limit. Journal of Fluid Mechanics 465, 261–291.

Campbell, C.S., 2003. A problem related to the stability of force chains. Granular Matter 5, 129–134.

Cundall, P.A., Strack, O.D.L., 1979. A discrete numerical model for granular assemblies. Geotechnique 29, 47–65.

Deshpande, V.S., Heaver, A., Fleck, N.A., 2006. An underwater shock simulator. Proceedings of the Royal Society of London A 462, 1021–1041.

Dharmasena, K.P., Queheillalt, D.T., Wadley, H.N.G., Dudt, P., Chen, Y., Knight, D., Evans, A.G., Deshpande, V.S., 2009a. Dynamic compression of metallic sandwich structures during planar impulsive loading in water. European Journal of Mechanics-A/Solids, in press, doi:10.1016/j.euromechsol.2009.05.003.

Dharmasena, K.P., Spuskanyuk, A., Wadley, H.N.G., McMeeking, R.M., Evans, A.G., Deshpande, V.S., 2009b. Loading of plates by spherically expanding shells of sand: experiments and simulation. Submitted for publication.

Drake, J.L., Little, C.D., 1983. Ground shock from penetrating conventional weapons. In: Proceedings of the Symposium on the Interaction of Non-nuclear Weapons with Structures, Colorado Springs, USA.

Drucker, D.C., Prager, W., 1952. Soil mechanics and plastic analysis or limit design. Quarterly of Applied Mathematics 10, 157–165.

Fleck, N.A., Deshpande, V.S., 2004. The resistance of clamped beams to shock loading. Journal of Applied Mechanics 71, 386–401.

Foedinger, J., 2005. Methodology for improved characterization of landmine explosions, SBIR Phase-II plus program. In: Proceedings of the Technical Interchange Meeting, Material Science Corporation.

Grujicic, M., Pandurangan, B., Cheeseman, B.A., 2006. The effect of degree of saturation of sand on detonation phenomena associated with shallow-buried and ground-laid mines. Journal of Shock and Vibration 13, 41–61.

Grujicic, M., Pandurangan, B., Qiao, R., Cheeseman, B.A., Roy, W.N., Skaggs, R.R., Gupta, R., 2008. Parameterization of the porous-material model for sand with different levels of water saturation. Soil dynamics and Earthquake Engineering 28, 20–35.

Jenkins, J.T., Savage, S.B., 1983. A theory for the rapid flow of identical, smooth, nearly elastic particles. Journal of Fluid Mechanics 130, 187–202.

Johnson, S.M., 1971. Explosive excavation technology. NCG Report No. 21, US Army Engineer Nuclear Cratering Group, Livermore, USA.

Kambouchev, N., Noels, L., Radovitzky, R., 2006. Compressibility effects on fluid–structure interactions and their implications on the blast loading of structures. Journal of Applied Physics 100, 063519.

Kingery, C.N., Bulmash, G., 1984. Air blast parameters from TNT spherical air burst and hemispherical surface burst. Technical Report ARBRL-TR-02555, AD-B082 713, US Army Ballistic Research Laboratory, Aberdeen Proving Ground.

Laine, P., Sandvik, A., 2001. Derivation of mechanical properties for sand. In: Proceedings of the Fourth Asia-Pacific Conference on Shock and Impact Loads on Structures. CI-Premier PTE LTD., Singapore, pp. 361–368.

Liang, Y., Spuskanyuk, A.V., Flores, S.E., Hayhurst, D.R., Hutchinson, J.W., McMeeking, R.M., Evans, A.G., 2007. The response of metallic sandwich panels to water blast. Journal of Applied Mechanics 74, 81–99.

Liepmann, H.W., Roshko, A., 2001. Elements of Gas Dynamics. Dover, New York.

Morris, B.L., 1993. Analysis of improved crew survivability in light vehicles subjected to mine blast. Final report for Contract No. DAAK70-92-C-0058 for the US Army Belvoir RDEC, Ft. Belvoir, VA.

Muir Wood, D., 1990. Soil Behaviour and Critical State Soil Mechanics. Cambridge University Press, UK.

Neuberger, A., Peles, S., Rittel, D., 2007. Scaling the response of circular plates subjected to large and close-range spherical explosions. Part II: buried charges. International Journal of Impact Engineering 34, 874–882.

Noels, L., Dharmasena, K.P., Wadley, H.N.G., Radovitzky R., 2009. Air shock loading of metallic plates: experiments and coupled simulations. International Journal of Solids and Structures, submitted for publication.

Press, F., 1966. Seismic velocities. In: Clark, Jr., S.P. (Ed.), Handbook of Physical Constants, Geological Society of America Memoir, vol. 97, pp. 97–173.

Roscoe, K.H., Schofield, A.N., Wroth, C.P., 1958. On the yielding of soils. Geotechnique 8, 22–53.
Tremblay, J.E., Bergeron, D.M., Gonzalez, R., 1998. Protection of soft-skinned vehicle occupants from landmine effects. The Technical Cooperation Program, Subcommittee on Conventional Weapons Technology, Technical Panel W-1, USA.
von Neumann, J., Richtmyer, R., 1950. A method for the numerical calculation of hydrodynamic shocks. Journal of Applied Physics 21, 232–237.
US Army Technical Manual, 1992. Fundamentals of protective design for conventional weapons. TM 5-855-1.
Wadley, H.N.G., Dharmasena, K., Chen, Y., Dudt, P., Knight, D., Charette, R., Kiddy, K., 2008. Compressive response of multilayered pyramidal lattices during underwater shock loading. International Journal of Impact Engineering 35, 1102–1114.
Wei, Z., Dharmasena, K.P., Wadley, H.N.G., Evans, A.G., 2007. Analysis and interpretation of a test for characterizing the response of sandwich panels to water blast. International Journal of Impact Engineering 34, 1602–1618.
Wei, Z., Deshpande, V.S., Evans, A.G., Dharmasena, K.P., Queheillalt, D.T., Wadley, H.N.G., Murty, Y., Elzey, R.K., Dudt, P., Chen, Y., Knight, D., Kiddy, K., 2008. The resistance of metallic plates to localized impulse. Journal of Mechanics and Physics of Solids 56, 2074–2091.
Wang, Z., Hao, H., Lu, Y., 2004. A three-phase soil model for simulating stress wave propagation due to blast loading. International Journal for Numerical and Analytical Methods in Geomechanics 28, 33–56.
Wang, Z., Lu, Y., 2003. Numerical analysis on dynamic deformation mechanisms of soils under blast loading. Soil Dynamics and Earthquake Engineering 23, 705–714.
Weckert, S., Andersen, C., 2006. A preliminary comparison between TNT and PE4 landmines. Report No. DSTO-TN-0723, Defence Science and Technology Organization, Edinburgh, South Australia.
Westine, P.S., Morris, B.L., Cox, P.A., Polch, E., 1985. Development of computer program for floor plate response from land mine explosions. Contract Report No. 1345 for US Army TACOM Research and Development Centre.